Study of thallium-zinc-tin-oxide semiconductor toward high mobility, stable thin-film transistors

高移動度・安定な薄膜トランジスタに向けた酸化タリウム・亜鉛・錫半導体の研究

Katsushi Kishimoto

Information Device Science Laboratory

Nara Institute of Science and Technology

Contents

Chapter 1 Introduction

1.5 Background information

The development of flat panel displays (FPDs), which utilize liquid crystal displays (LCDs) or organic luminance emission displays (OLEDs), is continuing towards large-area panels with high definition. In particular, the market for high-functioning displays has increased as a result of the growing global use of smart phones and tablets. As regards large-screen television (TV) panels, the LCD TV market has already become saturated, and the price competition in each panel-size category has increased severely because of less difference of product of each company. In addition, FPD product applications such as watch-type and other wearable devices have been introduced in recent years, in conjunction with the existing conventional flat televisions (TVs). These new applications are currently being developed through a trial-and-error process, which requires a number of years, and it appears that the market for these devices is forming. [1] In this environment, high-performance and high-definition displays are evolving gradually, and have become an essential technology for the development of applied products featuring FPDs. In particular, high-performance, cost-effective, and flexible OLED panels have been identified as a necessary next-generation technological innovation.

Among the various semiconductor materials, hydrogenated amorphous silicon (a-Si:H) has historically been employed to achieve thin-film-transistor (TFT) switching in flat panel displays (FPDs). Even today, a-Si:H TFTs are still used to drive large-area displays at low cost. [2] However, these TFTs are unable to meet the high mobility and high stability requirements of high-performance displays. It is expected that the transparent amorphous oxide semiconductor (AOS), which was developed by Hosono et al. in 2004, [3] will become the next mainstream TFT material. An AOS has high mobility and can be deposited easily a thin film on the large area glass by a sputtering process.

Therefore, the AOS is positioned as a promising candidate that can satisfy market requirements for an inexpensive and high-performance FPD driver. Almost all display manufacturing companies are engaging in active development toward the practical use of this material. [4-6] For example, a large-area LCD display employing InGaZnO (IGZO), which is referred to as the first-generation backplane, has been produced by the Sharp Corporation, [7] and a large-area OLED display that also employs IGZO has been produced by LG Electronics Inc. [8] However, IGZO, which has a carrier mobility of approximately 10 $cm^2V^{-1}s^{-1}$, does not meet the performance requirements for application in tablets and high-performance panels. Instead, low-temperature poly-silicon (LTPS) has been used in tablets and related devices, [9] as this material yields higher mobility and stability than IGZO. However, LTPS is a relatively expensive semiconductor material.

In order to produce an oxide semiconductor TFT suitable for practical application, stable mobility and reliability must be obtained. [10] These properties are heavily influenced by the choice of oxide semiconductor material, because the electronic state of the material affects the TFT performance. [11] In the case of IGZO, which has been used in practical production, In has an important influence on the exhibited high mobility, via the electrons in the 5s orbital. Therefore, In is one of the indispensable elements as regards high mobility. It is widely accepted that the most promising AOS materials are based on ternary systems that contain In, which yields improved field-effect mobility. This applies not only to the first-generation IGZO, but also to the second-generation InZnSnO (IZTO). IZTO TFTs exhibit excellent electrical performance, such as high field-effect mobilities of 21.7–51.7 $cm^2V^{-1}s^{-1}$. [12] [13] However, in the case of IZTO, the TFT characteristics are more sensitive to changes in the In electronic state, the nearby layers, and the surfaces in contact with different layer ; therefore, both the post-annealing treatment and deposition conditions can have a strong impact on the resultant TFT performance. [14]

Typically, in order to obtain large electron mobility in an AOS, a heavy metal ion having an S trajectory that is spatially dispersed as the lowest non-shared level, i.e., an In- or Sn-based material, is employed. In fact, amorphous thin films such as InSnO (ITO)- or SnO_2-based materials, the conduction band minimums (CBMs) of which are determined by the 5s orbitals of In or Sn, exhibit high mobility. For example, the mobility of epitaxially grown ITO has

been reported to be approximately 60 $cm^2V^{-1}s^{-1}$. [15] However, the mobility decreases with increased SnO_2 content, and is very sensitive to changes in the Sn composition. Fig. 1-1 shows the resistivity, Hall mobility, and carrier density of ITO thin film deposited on yttria-stabilized zirconia (YSZ) (100) as a function of the SnO_2 film content. [15] The O deficiency in the oxide semiconductor is known to significantly affect the electronic structure. The results of a first-principles electronic structure calculation of the O vacancies (Vo) of amorphous IGZO (a-IGZO) are shown in Fig. 1-2. [16] According to these results, the energy level of the highest occupied molecular orbital (HOMO) intersects with the conduction band. In addition, the Vo wave function extends over the entire space, including In, rather than being not localized in a particular defect location. Therefore, the In Vo operate as donors.

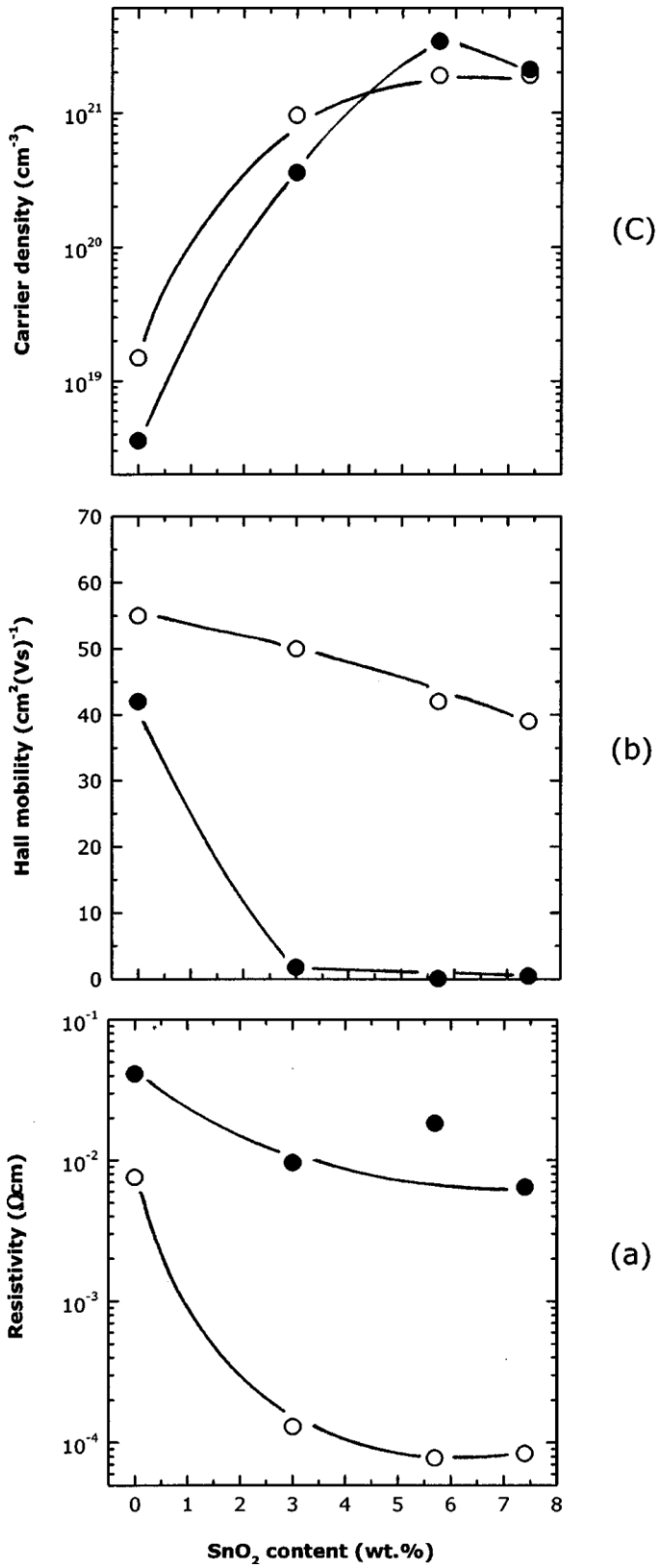

Fig. 1-1 Resistivity, Hall mobility, and carrier density of ITO thin film deposited on YSZ (100) as functions of SnO_2 film content. [○: ITO/YSZ, ●: ITO/SiO_2 glass] [15]

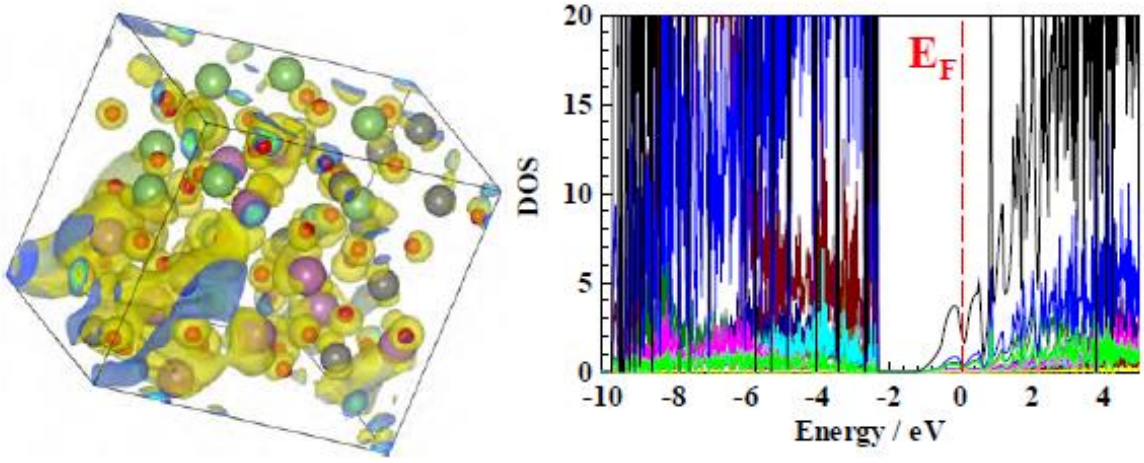

Fig. 1-2 Schematic diagram of wave function and density of states (DOS) of HOMO in a-$InGaZnO_4$ with O deficiency. The origin of the DOS energy is the Fermi level (E_F). [16]

It has also been reported that the carrier concentration of the high-quality (HQ) film by low pressure deposition that can be fabricated via pulsed laser deposition (PLD) differs significantly from that of a low-quality (LQ) film. [17] The mobility in the HQ film does not depend on temperature; however, that of the LQ film exhibits a thermal activation behavior. The relationship between the carrier density and Hall mobility for both the HQ and LQ films is shown in Fig. 1-3. [17] For the HQ film, it is apparent that the Fermi energy (E_F) is located beyond the valence band maximum (VBM) and that the carrier transport is little affected by the potential barriers. On the other hand, in the case of the LQ film, the higher density of the shallow trap level reduces the mobility through hopping transportation or percolation transportation between the trap level and VBM.

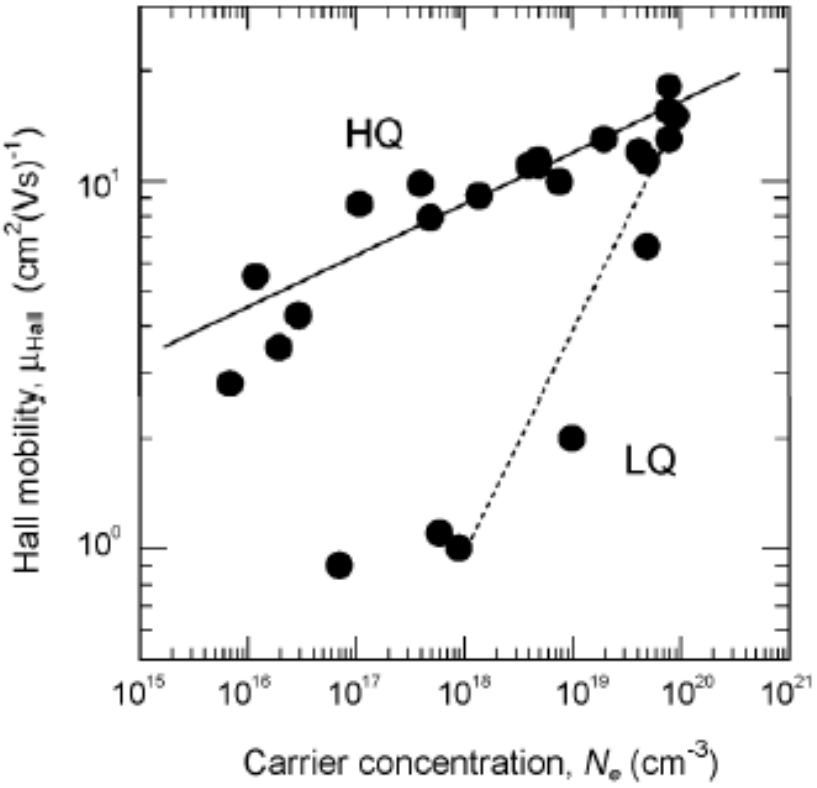

Fig. 1-3 Relationship between Hall mobility and carrier density in HQ and LQ films. [17]

Furthermore, the local coordination structures in both HQ and LQ films have been examined via fluorescence X-ray absorption fine structure (XAFS) measurements. [18] The dynamic size distribution functions (RDFs) of the In atoms in the HQ and LQ films, as measured via extended XAFTS (EXAFS) analysis, are shown in Fig. 1-4. [18] Both a strong first peak, which is attributed to the nearest O atom, and a weak second peak, attributed to the second neighboring atoms to the In atom, are apparent in the RDFs of both film types. Further, it is apparent that the In-In bonding length (0.318 ± 0.003 nm) in the HQ film differs from that of the LQ film (0.325 ± 0.003 nm). On the other hand, Zn and Ga can be observed in the first peak only, which is attributed to the O bond, and a clear difference between these results for both film types is not apparent. Thus, only the local structures in the vicinity of the In

atoms in the HQ film differ from those of the LQ film.

The above findings indicate that the In atoms are required in order for high mobility to be achieved. However, the electronic states of the In atom are very unstable, which has a significant effect on the electrical properties of In-based oxide semiconductors.

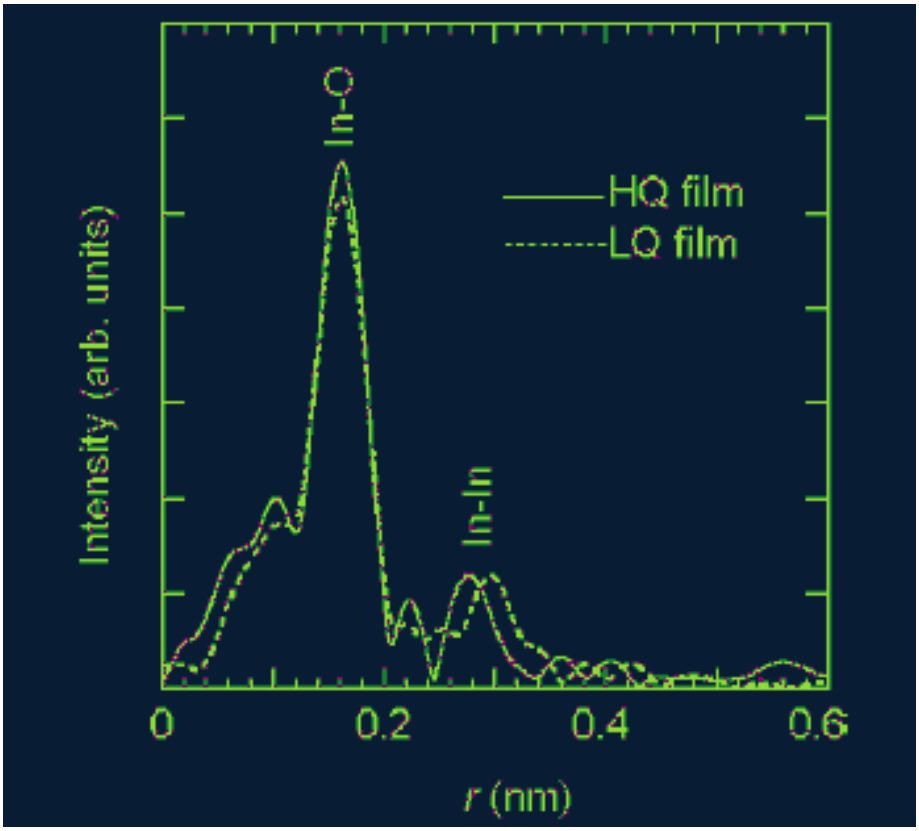

Fig. 1-4 RDFs of In atoms in HQ and LQ films. r shows a radius of each bond. [18]

In this study, the author has chosen to focus on Tl as a replacement for In in IZTO, i.e., TlZnSnO is examined as a second-generation AOS. The periodic table is shown in Fig. 1-5 [19]. and the ionization diameter of each element is indicated. Tl is in the same group 3B column as Al, Ga, and In, which are commonly used as oxide semiconductor materials. Tl has

the largest S orbital of 6s in group 3B. Note that a large ionization diameter is necessary for high TFT mobility via percolation electrical transformation. Thus, a Tl-based AOS can be expected to exhibit higher mobility than an In-based AOS. As regards the material cost, Tl is obtained via a Cu refining process, like In. Thus, the fabrication cost of a Tl-based AOS is expected to be similar to or less than that of In-based materials, for the same composition ratios.

Fig. 1-5 Periodic table showing element ionization diameters. [19]

In addition, high In composition causes instability of the electrical characteristics, as has been reported for a-IGZO, which is unstable because of the existing Vo. This explains why the Vo transition point from Vo^0 to Vo^{2+} is very close to the In_2O_3 bandgap at 2.67 eV, as the Vo defect varies between Vo^0 and Vo^{2+} easily in response to slight CBM level shifts (Fig. 1-6). [20]

It is strongly indicated that the larger Tl s orbital in TlZnSnO compared to the In s orbital in IZTO can yield superior field-effect mobility, according to the hypothesis presented by Hosono et al. [21] Fig. 1-7 shows the calculated Vo formation energies for Tl_2O_3 as functions of E_F. [22] The charged Vo defects in the Tl oxide material are significantly more stable than those of In, because it is difficult to move to the CBM [22] such that the Tl atom charge is adjusted from Tl^{2+} to Tl^0. As regards the production possibility of Tl materials, Tl-based materials have not been widely produced because of their toxicity. [23] On the other hand, Tl oxide is sufficiently stable to be utilized in semiconductor research and production. [24] [25] The above considerations influenced the selection of Tl for examination as a substitution element for In in IZTO in this study.

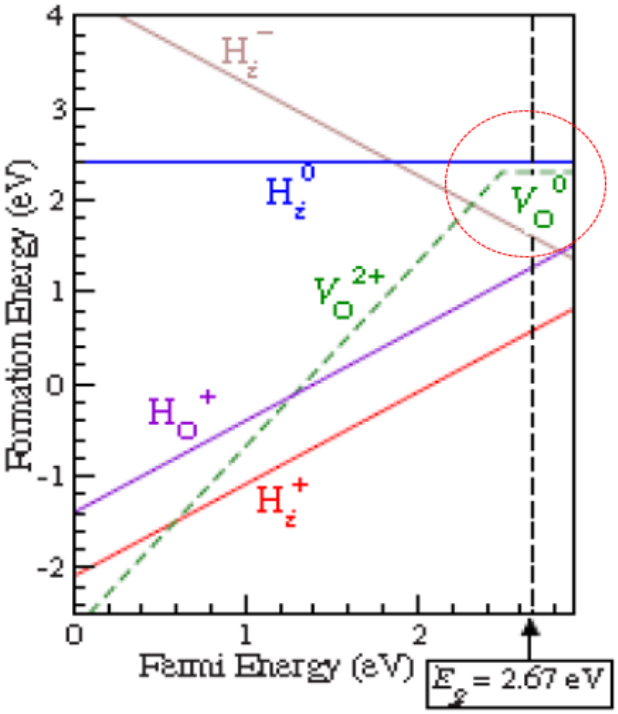

Fig. 1-6 Calculated formation energies of H defects and Vo in In_2O_3 as functions of E_F. [20]

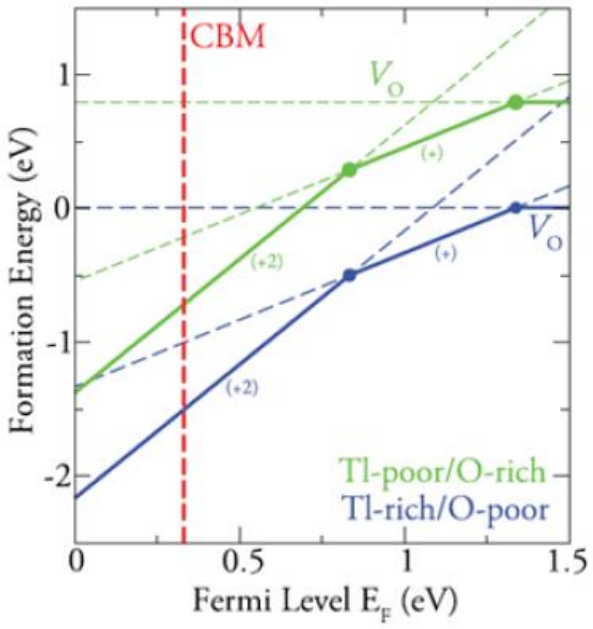

Fig. 1-7 Calculated formation energies of Vo in Tl_2O_3 as functions of E_F. [22]

1.2 Requirements for next-generation displays

The mobility of an a-Si:H semiconductor suitable for application in an FPD is approximately 0.5 $cm^2 (Vs)^{-1}$, for a film that is uniformly deposited on a large substrate. Therefore, this material has excellent mass productivity and is widely used in large panels for TFT backplanes. However, it is expected that next-generation large-panel TVs, i.e., those with 80-inch LCD displays and 120-Hz drives, will require high mobilities of more than 3 $cm^2 (Vs)^{-1}$. Furthermore, it is expected that transparent or flexible OLEDs will require significantly higher mobilities than TFT backplanes. [26-28] Previously, Matsueda et al. reported the relationship between the pixel number of a panel and the required mobility. [29] As shown in Fig. 1-8 (from [29]), new semiconductor materials with high mobility and low cost must be employed, because the conventionally used a-Si:H TFT with 0.5 $cm^2 (Vs)^{-1}$ constitutes a performance limitation. Note that LTPS, which are comprised of both an organic semiconductor and an oxide semiconductor, are semiconductor materials that potentially satisfy the requirements for commercialization.

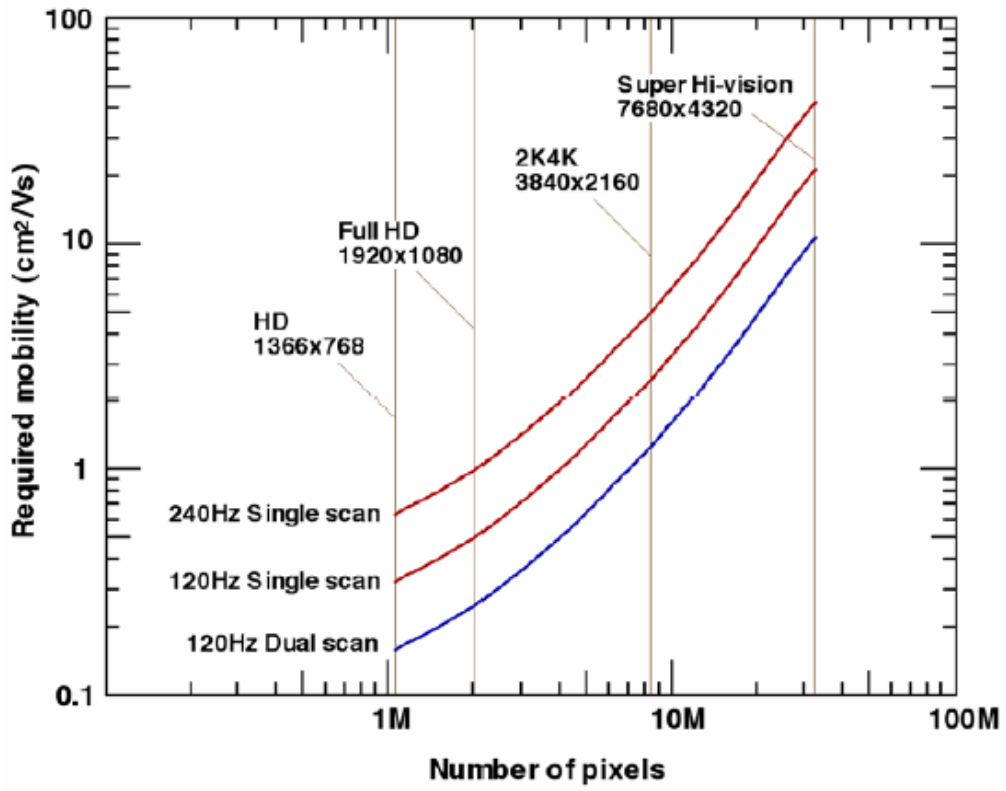

Fig. 1-8 Relationship between TFT mobility and required number of pixels for selected active frequencies. [29]

LTPS TFTs have excellent properties as regards both mobility and reliability; however, their manufacturing process is highly complex and costly. In particular, for large-area substrate mass-production employing an Exima-laser-annealing crystallization process, the equipment size limitation yields TFTs that are restricted to a substrate width of less than 1,500 mm. Currently, mass-production lines for G10.5-generation glass sizes over 3,000 mm width (used in large-area TVs) are being widely employed; therefore, the 1,500-mm TFT width restriction is an excessively large disadvantage in terms of mass production of low-cost panels. Furthermore, the LTPS TFT process temperature required for crystallization and activation is significantly higher than 400 °C; therefore, plastic substrates cannot be used. The wiring

material is also limited to a refractory metal. However, the resistivity of a refractory metal is considerably higher than that of Cu of Al, which are generally used for a-Si TFTs. Therefore, a number of device design issues must be considered, which also include yield reduction due to thickening of the layer. This issue is strongly dependent on the decreased aperture ratio and electrode losses caused by widening of the line width.

On the other hand, large-area fabrication can be achieved easily for organic semiconductors through printing or evaporation. In fact, intense research towards the achievement of higher mobilities of more than 10 $cm^2V^{-1}s^{-1}$ has already been conducted [30], and many researchers are working to enhance not only high mobility but high reliability of organic semiconductors. [31, 32] Nevertheless, significant problems remain as regards the reliability and reproducibility of these devices. [33] Moreover, organic-semiconductor technology requires further systematic improvement for mass-production, and additional technological developments are required in order to realize applications such as TFT devices for large-area TVs.

In contrast, oxide semiconductors can be easily deposited on a large-area substrate via a sputtering process, and the other processes may be mass-produced through processes that are almost analogous to those of an a-Si TFT production line. Furthermore, as the process temperature is relatively low, the fabrication of non-vacuum film through a solution process has become possible in recent years. [33] Such mass production is associated with cost

reduction, as the device structure is simpler than that of LTPS TFTs. Device stabilization must be achieved via heat treatment in the case of an oxide semiconductor; however, this is feasible and can be obtained at temperatures at 400 °C lower. In the field of material science and research, the current research trend has changed from a focus on first-generation IGZO to second-generation IZTO, and a large number of possible combinations of several elements have been examined, yielding significantly improved TFT characteristics like mobility and reliability. Thus, display makers are aggressively pursuing material research to identify new materials similar to IZTO. The characteristics of various relevant semiconductor materials are compared in Table 1-1.

Table 1-1 Characteristics of various semiconductor materials for displays.

	a-Si	**LTPS**	**Oxide semiconductor**	**Organic semiconductor**
Material	a-Si:H	poly-Si	IGZO, etc.	pentasen, etc.
Mobility $cm^2(Vs)^{-1}$	0.5	50–100	10–70	0.1–43
Productivity	G10.5 production	G5.5 production	8.5G production	none
Glass size	> G10	< G5.5	8.5G	none
Photo process number	less (4 mask)	less (> 8 mask)	less (5 mask)	none
Stability	poor	good	fair	poor
Process temp. (°C)	300	800–1000	< 400	100

1.3 Purpose

In this study, the author considers an effective solution that yields both high mobility and Vo stability in In-based oxide semiconductors, and introduces the possibility of Tl-based oxide semiconductors for use as channel materials in high-mobility and high-stability TFTs. Particular focus is placed on TlZnSnO.

1.4 Structure of this thesis

The structure of the present manuscript is as follows. In Chapter 2, the characteristics of XZnSnO TFTs are examined, where X corresponds to Al, Ga, or In (group 3B materials), in order to determine the expected TlZnSnO TFT performance (as Tl is also a member of group 3B). In Chapter 3, a first-principles simulation is attempted in order to estimate the TlZnSnO performance and determine the TFT mobility. This performance is considered to be related to the nature of the Tl-Tl bond for Tl concentrations of 30 and 40%. It can be anticipated that the 6s orbital of the Tl atom generates high electron mobility, based on the percolation transportation model. In Chapter 4, a TlZnSnO target is prepared by confirming a suitable annihilation route for higher-stability TlZnSnO. First, the author confirms the reactivities of various metal oxides, i.e., Tl_2O_3 and ZnO, SnO_2, or In_2O_3, so as to anticipate the affinity of Tl with Zn, Sn, or In. Then, the author determines the appropriate calcination process for

TlZnSnO. In Chapter 5, TlZnSnO films are fabricated via sputtering of a TlZnSnO target. This clarifies the manner in which the partial O_2 pressure (relative to the total pressure) influences the optical and electrical film properties of the fabricated TlZnSnO.

References

[1] ex.: http://www.apple.com/watch/
[2] Improved a-Si: H TFT pixel electrode circuits for active-matrix organic light emitting displays, Y He, R Hattori, J Kanicki, IEEE Transactions on Electron Devices 48, No. 7, 1322 (2001).
[3] Room-temperature fabrication of transparent flexible thin-film transistors using amorphous oxide semiconductors, K Nomura, H Ohta, A Takagi, T Kamiya, M Hirano, Nature 432, 488 (2004).
[4] Negative-bias photodegradation mechanism in InGaZnO TFT, M Tsubuku, R Watanabe, N Ishihara, H Kishida, M Takahashi, S Yamazaki, Y Kanzaki, H Matsukizono, S Mori, T Matsuo, SID Symposium Digest of Technical Papers 44, Issue 1, 166 (2013).
[5] Electronic transport properties of amorphous indium-gallium-zinc oxide semiconductor upon exposure to water, J-S Park, J K Jeong, H-J Chung, Y-G Mo, H D Kim, Applied Physics Letters 92, 072104 (2008).
[6] Technological progress and commercialization of OLED TV, C-H Oh, H-J Shin, W-J Nam, B-C Ahn, S-Y Cha, S-D Yeo, SID Symposium Digest of Technical Papers 44, Issue 1, 239 (2013).
[7] Development of IGZO-TFT and creation of new devices using IGZO-TFT, Y Kataoka et al., SID Symposium Digest of Technical Papers 44, Issue 1, 771–774 (2013)
[8] Novel technologies for commercialized 55-inch WRGB OLED TV, YH Tak et al., Proceedings of SPIE 8829, Organic Light Emitting Materials and Devices XVII, 88290R (2013).
[9] LTPS based transparent AM OLED, Y W Song, K H Hwang, S G Yoon, J H Ha, K N Kim, J H Lee, S C Kim, SID Symposium Digest of Technical Papers 41, Issue 1, 144 (2010).
[10] Present status of amorphous In–Ga–Zn–O thin-film transistors, T Kamiya, K Nomura, H Hosono, Science and Technology of Advanced Materials 11, 044305 (2010).
[11] High-performance thin film transistor with amorphous In2O3–SnO2–ZnO channel layer, S Tomai, M Nishimura, M Itose, M Matuura, M Kasami, S Matsuzaki, H Kawashima, F Utsuno, K Yano, Japanese Journal of Applied Physics 51, 03CB01 (2012).
[12] High mobility oxide semiconductor TFT for circuit integration of AM-OLED, E Fukumoto, T Arai, N Morosawa, K Tokunaga, Y Terai, T Fujimori, S Sasaoka, Proceedings of 17th International Display Workshops, 631 (2010).
[13] Influence of active layer thickness on performance and reliability of InSnZnO thin-film transistors, D Wang, C Li, M Furuta, S Tomai, M Sunagawa, M Nishimura, E Kawashima, M Kasami, K Yano, Proceedings of the 20th International Workshop on Active-Matrix Flatpanel

Displays and Devices, 159 (2012).
[14] Achieving high field-effect mobility exceeding 50 cm/Vs in In-Zn-Sn-O thin-film transistors, J H Song et al., Electron Device Letters, IEEE 35, Issue 8, 853 (2014).
[15] Highly electrically conductive indium–tin–oxide thin films epitaxially grown on yttria-stabilized zirconia (100) by pulsed-laser deposition, H Ohta, M Orita, M Hirano, H Tanji, H Kawazoe, H Hosono, Applied Physics Letters, 76, No. 19, 2740 (2000).
[16] Electronic structure of oxygen deficient amorphous oxide semiconductor a-$InGaZnO_{4-x}$: Optical analyses and first-principle calculations, T Kamiya, K Nomura, M Hirano, H Hosono, Physica Status Solidi 5, 3098 (2008).
[17] Relationship between non-localized tail states and carrier transport in amorphous oxide semiconductor, In–Ga–Zn–O, K Nomura, T Kamiya, H Ohta, K Shimizu, M Hirano, H Hosono, Physica Status Solidi (a) 205, 1910 (2008).
[18] Present status of amorphous In–Ga–Zn–O thin-film transistors, T Kamiya, K Nomura, H Hosono, Science and Technology of Advanced Materials, 11, 044305 (2010).
[19] https://www.pinterest.com/pin/28006828904172302/
[20] Hydrogen doping in indium oxide: An ab initio study, S Limpijumnong, P Reunchan, A Janotti, C G van de Walle, Physical Review B 80, 193202 (2009).
[21] Novel oxide amorphous semiconductors: transparent conducting amorphous oxides, H Hosono, N Kikuchi, N Ueda, H Kawazoe, Journal of Non-Crystalline Solids 198–200, 165 (1996).
[22] Nature of the band gap of Tl2O3, A B Kehoe, D O Scanlon, G W Watson, Physical Review B 83, 233202 (2011).
[23] K Kameda, Y Yoshida, S Sakairi, Nihon Kinzoku Gakkaishi 47, 406 (1983) [in Japanese].
[24] Efficient thallium photo dissociation laser, D J Ehrlich, J Maya, R M Osgood, Jr., Applied Physics Letters 33, 931 (1978).
[25] Gain in a thallium iodide laser with external resonator, P Burkhard, W Lüthy, T Gerber, Optics Letters 5, 522 (1980).
[26] Taishiro Kurita, “Tyoukouseisai kougashitu eizoukaihatuno syouraitennbou” ISTF 2008 symposium
栗田泰市郎、 “超高精細、高画質映像開発の将来展望“、 ISTF 2008 シンポジウム公演
[27] Mamoru Furutaet al., Kouchikoukadaigaku Kiyou 6(1), 41-45, (2009)
古田 守 他、 高知工科大学紀要、 6(1), 41-45, (2009)
[28] 2012～2014 nendo NHK Giken 3 kanen keikaku Fujisawa Shuichi R&D, No.135, 2, (2012)
2012～2014 年度 NHK 技研３か年計画 藤沢秀一、 NHK 技研 R&D, No.135, 2, (2012)

[29] Required characteristics of TFTs for next generation flat panel display backplanes, Y Matsueda, 6th International TFT Conference, 314 (2010).
[30] Ultra-high mobility transparent organic thin film transistors grown by an off-centre spin-coating method, Y Yuan, G Giri, A L Ayzner, A P Zoombelt, S C B Mannsfeld, J Chen, D Nordlund, M F Toney, J Huang, Z Bao, Nature Communications 5, 3005 (2014) doi:10.1038/ncomms4005.
[31] Bistetracene: An air-stable, high-mobility organic semiconductor with extended conjugation, L Zhang et al., Journal of the American Chemical Society, 136 (26), 9248 (2014).
[32] Fully solution-processed flexible organic thin film transistor arrays with high mobility and exceptional uniformity, K Fukuda et al., Scientific Reports, 4, 3947 (2014).
[33] Systematic reliability study of top-gate p- and n-channel organic field-effect transistors, D K Hwang et al., ACS Applied Materials and Interfaces, 6(5), 3378 (2014).
[34] Low-operating-voltage solution-processed InZnO thin-film transistors using high-k $SrTa_2O_6$, L Lu, Y Miura, T Nishida, M Echizen, Y Ishikawa, K Uchiyama, Y Uraoka, Japanese Journal of Applied Physics, 51, 3S (2012).

Chapter 2 Characteristics of TFTs with Group 3B materials Al, Ga, and In in ZnSnO, indicating TlZnSnO TFT performance

2.1 Introduction

According to Hosono et al., a transparent amorphous oxide semiconductor (TAOS) has a > 3.0-eV bandgap and electrical conductivity of 10 $cm^2V^{-1}s^{-1}$. [1] A high-mobility semiconductor can be fabricated using simple techniques such as sputtering or laser ablation deposition (LAD), which is why large flat-panel-display (FPD) mass production is feasible. The high electron mobility is due to features of the electronic structure caused by ionic bonding, and differs significantly from that of the electrically conductive structure of well-known strongly covalent semiconductors such as Si or GaAs. Fig. 2-1 is a schematic diagram of the bonding with electrical carrier path for Si and an oxide semiconductor. [2]

For Si, a bandgap of 1.1 eV is formed by the energy division between the binding of the sp^3 hybridized orbital and the anti-bonding orbital. Thus, the sp^3 hybrid orbital with strong spatial directivity forms both the lower edge of the conduction band (conduction band maximum: CBM) and the upper end of the valence band (valence band maximum: VBM), creating a conductive path for the transported carriers.

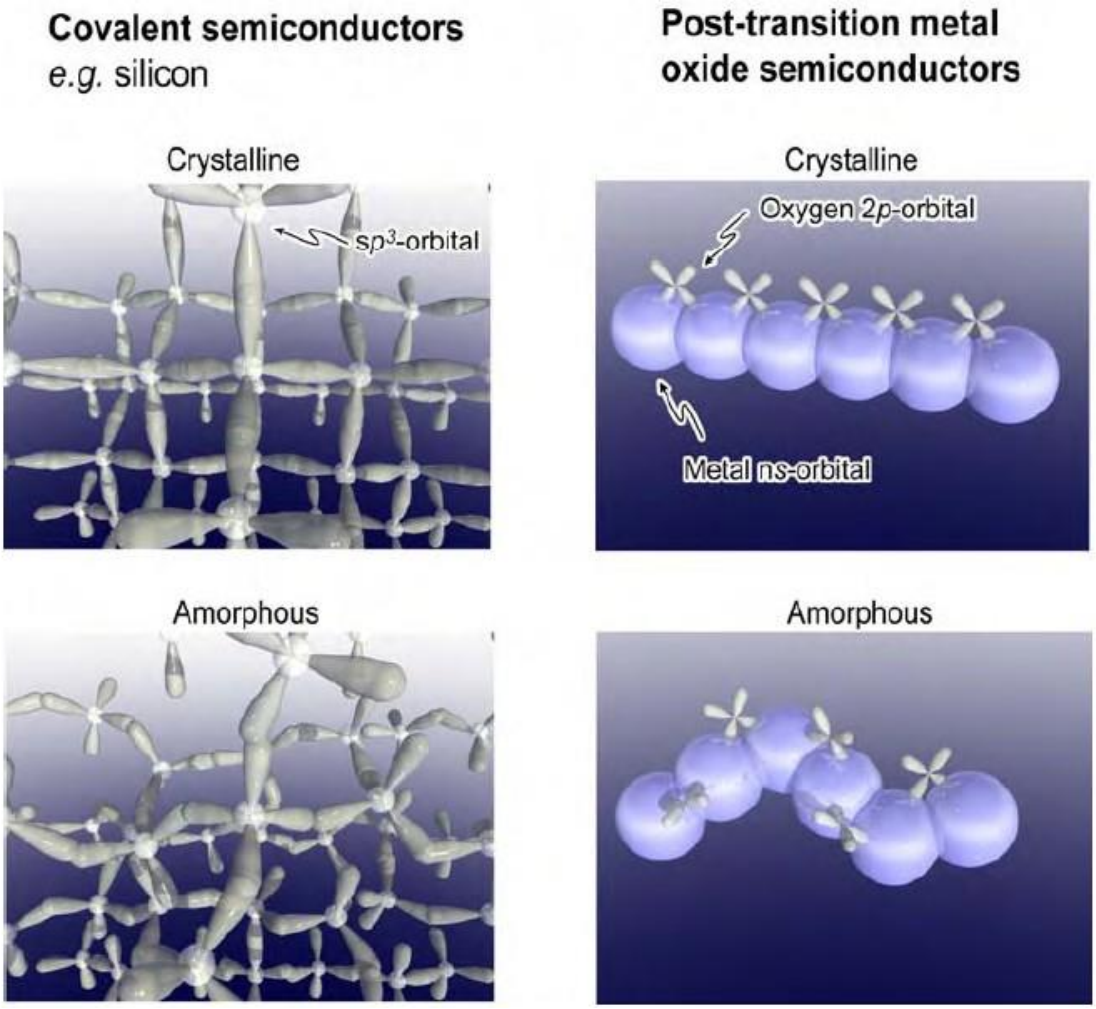

Fig. 2-1 Schematic diagram of the bonding with electrical carrier path for Si and oxide semiconductor. [2]

However, in the case of a hybridized sp^3 orbital with high directivity, structural disorder of the amorphous phase (as seen in a-Si) affects the electronic structure significantly. Thus, the carriers are localized through the formation of high densities of state (DOSs) below the valence band or above the conduction band. As a result, the a-Si mobility is lower than that of Si, being 1 cm^2V^{-1} s^{-1} or 1/1000th the mobility of single-crystalline Si. On the other hand, for an AOS, the electrostatic potential created by each ion in the crystal structure decreases the energy level of a pulse-charged ion. Therefore, a stabilized ionic crystal is obtained by

lowering the energy levels of the oxide ions. As a result, the 2p orbitals of the O ions determine the CBM in an AOS, whereas the non-occupied s orbitals of the positive ions determine the VBM. Thus, the bandgap of such an oxide semiconductor is determined by the electrostatic potential, which is not determined by the electron affinity only, but is also influenced by the ionization energy of each ion. In addition, as the wide spherical distributions of the *n* s orbitals (*n* is the principal quantum number) form the carrier transportation pathway of the electrons, neither the orbital overlap nor the carrier transportation are significantly affected by the distorted chemical bonds of the amorphous structure. Thus, the AOS can maintain high mobility despite its amorphous structure.

Correlation diagrams for (a) the Hall mobility and carrier density composition and (b) the phase structure for thin films in the In_2O_3-ZnO-Ga_2O_3 ternary system fabricated at room temperature (RT) are shown in Fig. 2-2. [3] All the examined films were fabricated via pulsed laser deposition (PLD) at RT with an O_2 partial pressure of 1 Pa. It is also known that the films prepared via sputtering methods exhibit the same dependencies of varius process parameter like pressure and substrate temperature so on. In_2O_3 or a thin film with a similar composition can achieve high electron mobility of more than 20 $cm^2V^{-1}s^{-1}$ in the case of RT deposition. [4] However, it is difficult for a stable amorphous film to form, in which the films must obtain a polycrystalline phase containing fine grain boundaries. [5] It has also been reported that amorphous thin film with a composition in the vicinity of Ga_2O_3 can be obtained

relatively easily; however, it is extremely difficult to realize such a film with a high carrier concentration. [6] Thus, it is difficult to form a stable oxide semiconductor using In_2O_3-ZnO-Ga_2O_3 films with similar compositions.

On the other hand, for the In_2O_3-ZnO (a-IZO) and In_2O_3-Ga_2O_3 (a-IGO) binary systems or the a-IGZO ternary system, stable amorphous thin films are formed over a wide composition range. For example, a-IZO thin films with high mobilities of approximately 40 cm^2V^{-1} s^{-1} have been obtained, along with a-IGO and a-IGZO-based thin films with high mobilities of approximately 20 cm^2V^{-1} s^{-1}. [7]

In the case of IGZO, it is well known that the In atoms influence the increased film mobility, and first-principles calculations show that these characteristics depend on the In 5s orbital. [8] On the other hand, in the case of the IZTO system, several high-mobility films have been reported [9-11]. However, the manner in which the In 5s orbital affects the film mobility has not been clarified in that case.

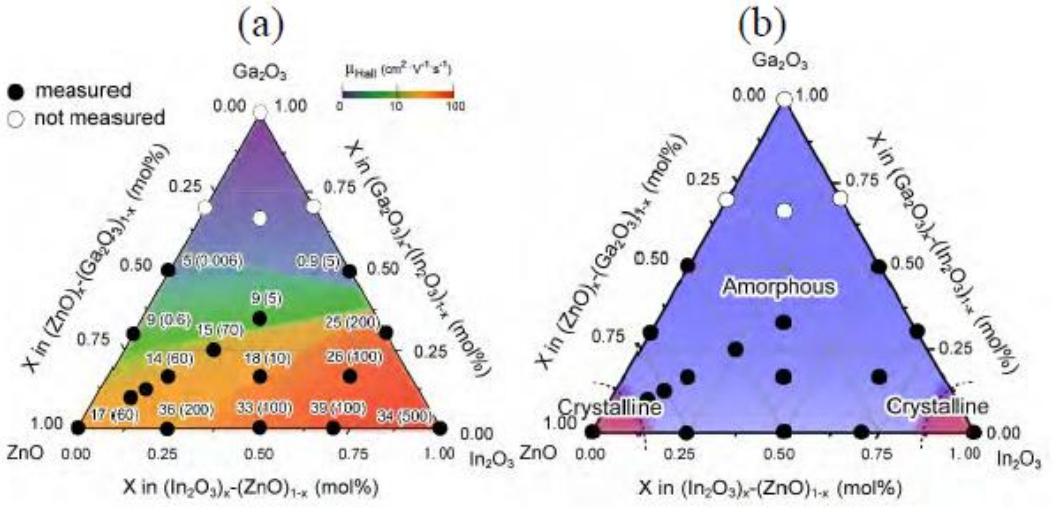

Fig. 2-2. Correlation diagrams for (a) Hall mobility and carrier density compositions and (b) phase structures of thin films in In_2O_3-ZnO-Ga_2O_3 ternary system fabricated at RT [3].

In this chapter, Al, Ga, or In, which have differently sized spherically symmetric s orbitals, are introduced to $Zn_{0.6}Sn_{0.4}O$ (ZTO). TFTs comprising XZnSnO (X = Al, Ga, or In) are fabricated and the linear TFT mobilities are compared. Then, the influence of the different s-orbital sizes of the group 3B elements on the TFT mobility is discussed. In Chapter 3, the effects of Tl (which has the maximum number of s orbital electrons of the group 3B elements, i.e., 6) on the TFT mobility are predicted. In experiment, the TFT characteristics for X = Al, Ga, and In in XZnSnO are compared each other to anticipate the Tl characteristics in XZnSnO and the TlZnSnO TFT performance.

2.2 Experimental

A 6-in.-diameter (Φ) highly doped n^{++} Si wafer substrate (resistivity: 0.5 Ωcm) with 1-mm thickness was prepared as a gate electrode, and a gate insulator comprised of an SiO_2 layer with 20-nm thickness was formed via thermal chemical vapor deposition (CVD). Three 4-in.Φ targets were employed, i.e., ZnO, $Zn_{0.6}Sn_{0.4}O$ (Zn:Sn = 6:4; ZTO), and X_2O_3 (X = Al, Ga, or In). Each XZnSnO channel layer (thickness = 100 nm) was deposited at RT using co-sputtering equipment, as shown in Fig. 2-3 (a). As the three target sources were simultaneously sputtered with an O_2/Ar gas ratio of 1/24, the XZnSnO film composition changed gradationally in the substrate regions located within the red circle in Fig. 2-3 (a). Hence, the TFT characteristics of XZnSnO with a wide range of X, Zn, and Sn composition ratios and on the same substrate could be estimated. In addition, a reference ZTO sample was also obtained by co-sputtering two targets using the same composition. Figure 2-3 (b) shows the schematic of the bottom-gate and top-contact XZnSnO TFT structure. Post annealing at 350 °C after active layer patterning via wet etching was conducted for 1 h in dry air. The source and drain metal was Ti, which had 100-nm thickness and was deposited via sputtering. The passivation layer was comprised of SiO_x (200 nm)/SiN_x (150 nm) and was continuously deposited in this order via plasma-enhanced (PE) CVD at a substrate temperature of 150 °C after N_2O plasma irradiation. Through-hole etching was performed using Ar/CHF_3 gases as etchant. The channel width and length (*W* and *L*, respectively) were designed to be 210 and 10

μm, respectively. The transfer characteristics for each TFT were measured using an auto prober for 272 points on 6-in.Φ wafers in darkness and air, at RT.

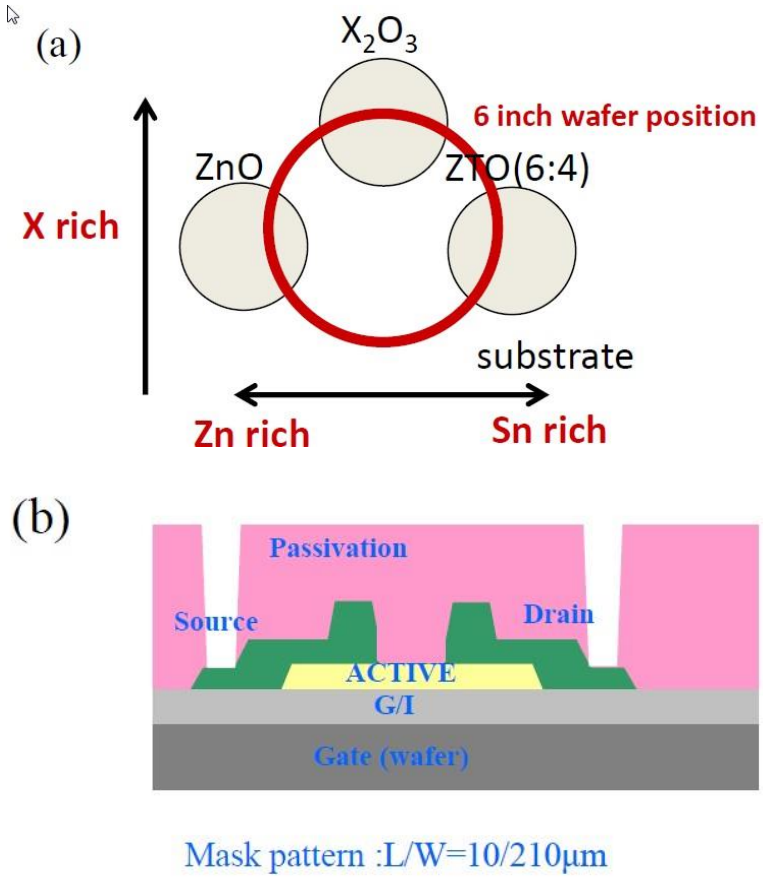

Fig. 2-3. (a) Co-sputtering target layout in process chamber and (b) schematic of bottom-gate, top-contact XZnSnO TFT structure.

2.3 Results and discussion

2.3-1 Distribution of TFT characteristics in XZnSnO [X =Al, Ga, and In]

Figure 2-4 shows 272-point mappings of the linear mobilities obtained from the transfer curves of each of the examined XZnSnO [X = (a) Al, (b) Ga, and (c) In] and (d) ZTO TFTs. All data were derived from the second scans of doubly scanned transfer curves, in order to confirm the TFT stability. The scanning voltage was set at a gate voltage (V_g) of −30 to +30 V and a drain voltage (V_d) of 10 V. It was first noted that the mobility distribution for the ZTO TFT (Fig. 2-4(d)) was sufficiently small to confirm the TFT mobility trend in response to changes in the XZnSnO composition on 6-in. wafers. Further, it was found that the semiconductor characteristics for each X element did not appear close to those of the ZnO target, even when V_g = −30 V, as shown by the black regions in Figs. 2-4 (a)–(c). It is thought that the additional Zn atoms induced a higher electrical charge and generated metallic electrical properties in all examined cases. [12] Increased TFT mobility was observed for the ZnSnO structure, compared to the base TFT mobility of ZTO of 13–17 cm^2V^{-1} s^{-1} (Fig. 2-4 (d)); however, the Al 3s and Ga 4s orbitals were not the primary sources of this increase, because the TFT mobilities of AlZnSnO and GaZnSnO decrease in response to increase Al and Ga compositions, as shown in Figs. 2-4 (a) and (b). In particular, heavy Al doping severely reduced the TFT mobility. As reported by Benwadih et al., the introduction of atoms with relatively large ionic radii decreases the carrier concentration, leading to a decrease in

mobility. [13] The present author also confirmed that the optimal Zn-to-Sn ratio for attaining a TFT mobility higher than that of $Zn_{0.6}Sn_{0.4}$ is within the Zn-rich region, i.e., the central parts of the contour plots shown in Figs. 2-4 (a) and (b). In particular, low Al and Ga ratios in the Zn-rich region, corresponding to the lower central regions of Figs. 2-4 (a) and (b), yielded the highest mobility. On the other hand, for IZTO, the TFT mobility increased gradually with increased In composition. This behavior clearly differs from that of both AlZnSnO and GaZnSnO, because the In 5s orbital contributed to the increased TFT mobility in the ZnSnO structure.

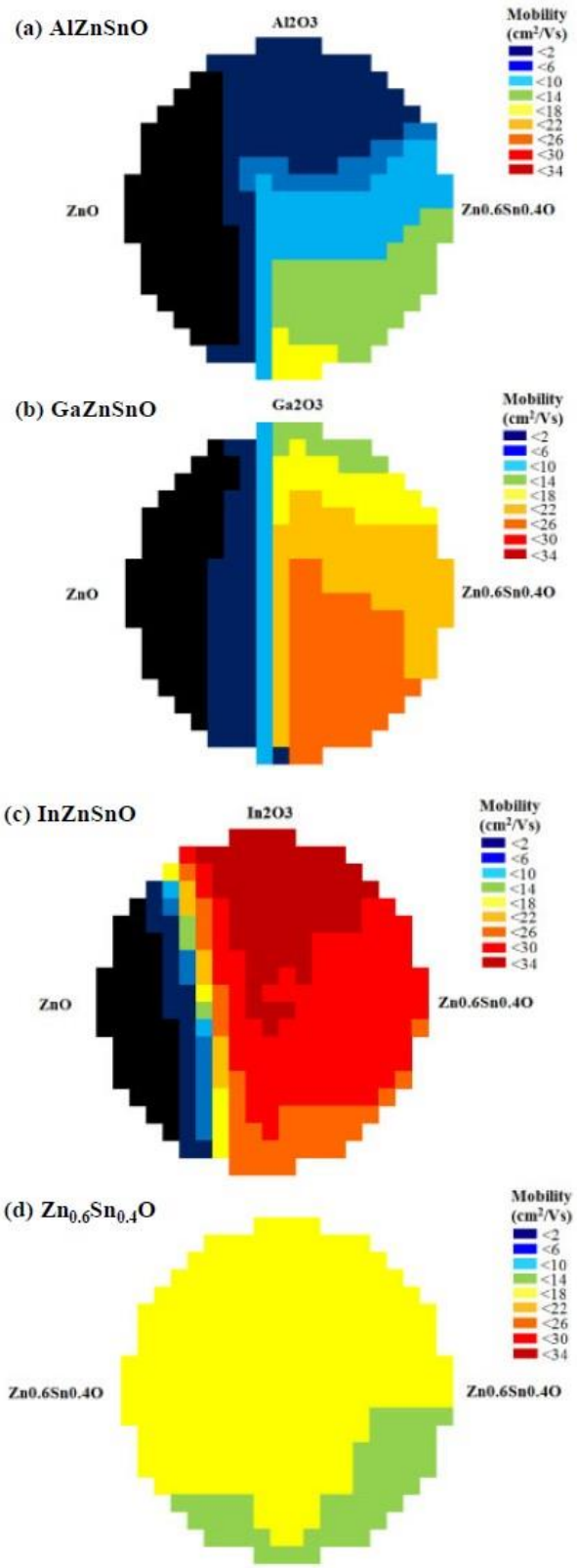

Fig. 2-4. 272-point distribution mapping of linear mobilities on wafer for XZnSnO [X = (a) Al, (b) Ga, and (c) In] TFTs and (d) ZTO TFT (for reference).

2.3-2 Highest TFT mobility in XZnSnO [X = Al, Ga, and In]

Table 1 and Figure 2-5 show the highest mobility performance characteristics of the XZnSnO TFTs. In the case of AlZnSnO, the highest mobility (14.4 cm^2V^{-1} s^{-1}) was obtained for a small Al content of 2 %. For GaZnSnO, the mobility gradually reduced with increased Ga composition, and the highest value of 25.6 cm^2V^{-1} s^{-1} was obtained for a low Ga composition of 10 %. In the case of IZTO, the mobility gradually varied from 23.0 to 32.0 cm^2V^{-1} s^{-1} with increased In composition. The highest TFT mobility for IZTO (32.0 cm^2V^{-1} s^{-1}) exhibited excellent properties such as a subthreshold swing (SS) of 0.3 V/decade and a threshold voltage (V_{th}) of −2.0 V, and was obtained for a high In composition of 40 %. The off-current level of the IZTO TFT was kept below 10^{-11} mA/cm^2, even at a V_g of −30 V (Fig. 2-5), and did not depend on the In content when this value was more than 40 % (not shown). It is expected that the off-current level of the TlZnSnO TFT will also be independent of the Tl content. The author experimentally confirmed that the size of the s orbital of element X strongly affected the TFT mobility in the XZnSnO co-sputtering system, as hypothesized by Hosono et al. [14] It is also clear that the strong effect of the X s-orbital size on the TFT mobility does not depend on any deposition or post-annealing conditions.

Table 1. Most suitable TFT parameters observed for XZnSnO (X = Al, Ga, In).

	Mobility (cm^2/Vs)	Ion at 30 V (A)	V_{th} at 1 nA (V)	*SS* value (V/decade)
$Al_{0.02}ZnSnO$	14.4	7.1E-04	1.5	0.3
$Ga_{0.10}ZnSnO$	25.6	1.4E-03	-2.7	0.4
$In_{0.40}ZnSnO$	32.0	2.3E-03	-2.0	0.3

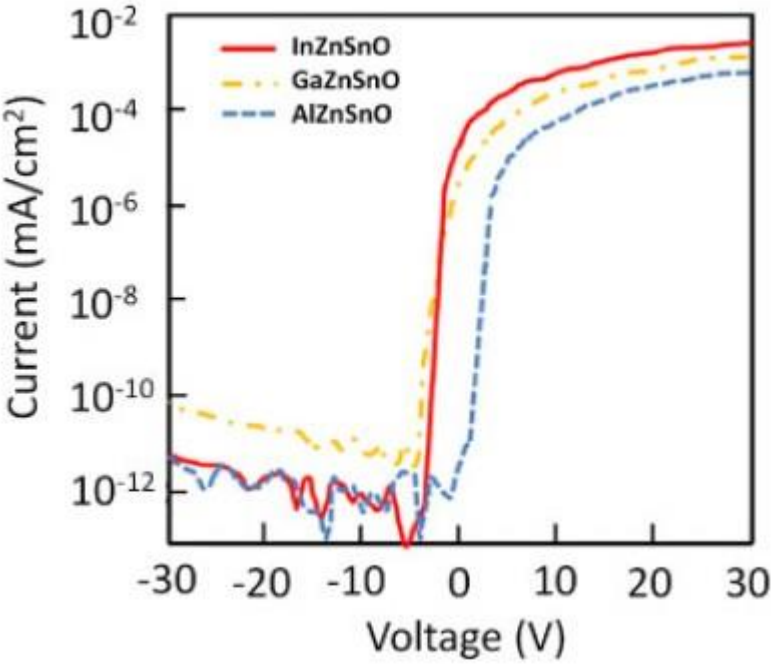

Fig. 2-5. Transfer characteristics of AlZnSnO, GaZnSnO, and IZTO TFTs. The blue dashed, yellow dot-dashed, and red solid lines show the AlZnSnO, GaZnSnO, and IZTO TFT characteristics, respectively.

The purpose of this chapter is both to confirm the role of the X s orbital in XZnSnO on the mobility and to predict the highest TFT mobility for the TlZnSnO system. Based on the observed results, it has been clarified that the X s-orbital size affects the TFT mobility, similar to In in the case of IGZO, and that a larger X s orbital is expected to yield higher TFT mobility. The relationship between the highest TFT mobility and the X s-orbital size for

XSnZnO, where X now indicates Al, Ga In, or Tl, is shown in Fig. 2-6. Hence, TlZnSnO TFT is expected to exhibit a higher mobility than XSnZnO (X = Al, Ga or In), because Tl has the largest s orbital of the group 3B elements. In addition, the mobility of the TlZnSnO TFT is expected to be more than 40 $cm^2V^{-1}s^{-1}$, assuming that the TFT mobility has a proportional relationship with the size of the s orbital similar to that of the other group 3B elements.

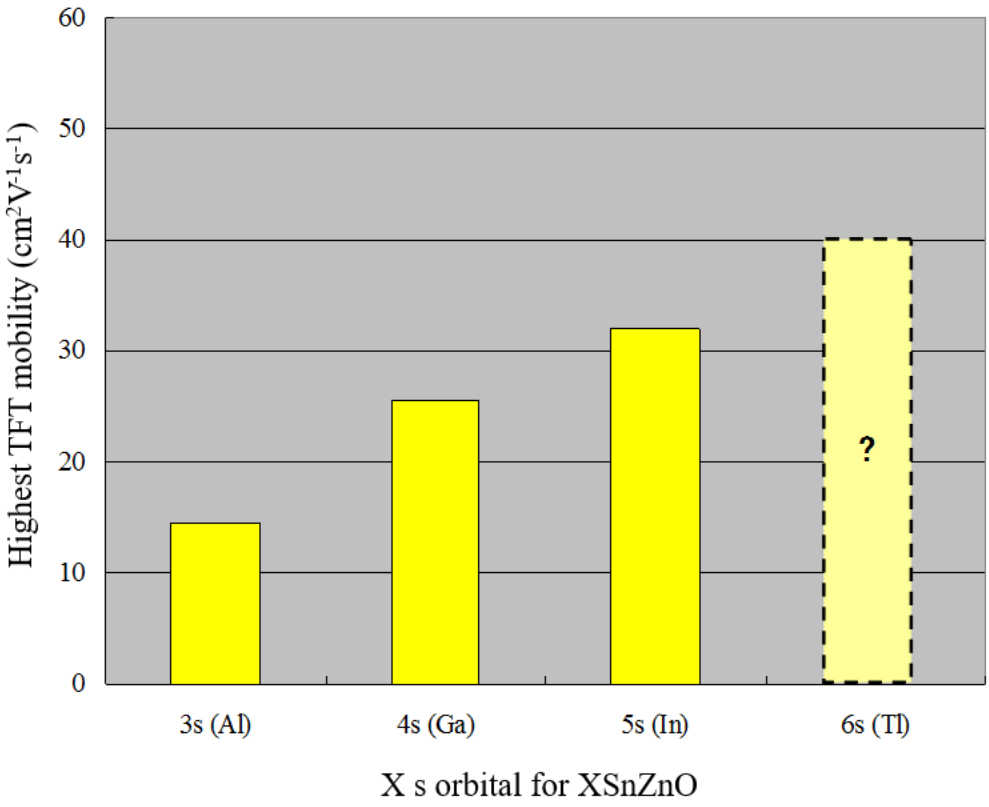

Fig. 2-6. Relationship between highest TFT mobility and X s-orbital size for XSnZnO (X = Al, Ga, In, or Tl).

2-4. Conclusion

In this chapter, the possible carrier mobility of TlZnSnO was predicted based on the estimated TFT mobilities of AlZnSnO, GaZnSnO, and InZnSnO. The highest TFT mobility was obtained for InZnSnO, at 32.0 cm^2V^{-1} s^{-1}, where excellent properties such as an SS of 0.3 V/decade and a V_{th} of −2.0 V were observed for a high In content of ~40 %. The off-current level of the InZnSnO TFT remained below 10^{-11} mA/cm^2, even at a V_g of −30 V, and was independent of the In content when that value was more than 40 %. These results suggest that the TlZnSnO TFT can yield a higher mobility than XSnZnO (X = Al, Ga, or In). The author experimentally confirmed that the size of the X s orbital strongly affects the TFT mobility in the XZnSnO co-sputtered system, as hypothesized by Hosono et al. It is possible that $Tl_{0.4}$ZnSnO has the highest mobility of the XSnZnO (where X is now Al, Ga, In, or Tl), at more than 40 cm^2V^{-1} s^{-1}. This prediction is based on the 6s orbital of Tl (larger than the In 5s orbital) for the same Zn and Sn content as $In_{0.4}$ZnSnO, which has 32.0-cm^2V^{-1} s^{-1} TFT mobility. [15]

References

[1] Present status of amorphous In–Ga–Zn–O thin-film transistors, T Kamiya, K Nomura, and H Hosono, Science and Technology of Advanced Materials 11, 044305 (2010).
[2] Recent progress in transparent oxide semiconductors: Materials and device application, H Hosono, Thin Solid Films 515, 6000 (2007).
[3] Ionic amorphous oxide semiconductors: Material design, carrier transport, and device application, H Hosono, Journal of Non-Crystalline Solids 352, 9–20, 851 (2006).
[4] Highly electrically conductive indium–tin–oxide thin films epitaxially grown on yttria-stabilized zirconia (100) by pulsed-laser deposition, H Ohta, M Orita, M Hirano, H Tanji, H Kawazoe, H Hosono, Applied Physics Letters 76, 2740 (2000).
[5] The electronic properties of amorphous and crystallized films, H Nakazawa, Y Ito, E Matsumoto, K Adachi, N Aoki, Y Ochiai, Journal of Applied Physics 100, 093706 (2006).
[6] Electron mobility in single and polycrystalline Ga_2O_3, M Fleischer, H Meixner, Journal of Applied Physics 74, 300 (1993).
[7] High mobility a-IGO films produced at room temperature and their application in TFTs, G Gonçalvesa, P Barquinha, L Pereira, N Franco, E Alves, R Martins, E Fortunato, Electrochemical and Solid-State Letters 13, 1, H20 (2010).
[8] Origins of high mobility and low operation voltage of amorphous oxide TFTs: Electronic structure, electron transport, defects and doping, T Kamiya, K Nomura, H Hosono, Journal of Display Technology 5, 7, 273, (2009).
[9] High mobility oxide semiconductor TFT for circuit integration of AM-OLED, E Fukumoto, T Arai, N Morosawa, K Tokunaga, Y Terai, T Fujimori, S Sasaoka, Proceedings of the 17th International Display Workshops 631 (2010).
[10] Thermal degradation and theoretical analysis of amorphous oxide thin-film transistor, D Wang, C Li, M Furuta, S Tomai, M Sunagawa, M Nishimura, E Kawashima, M Kasami, K Yano, Proceedings of the 20th International Workshop on Active-Matrix Flatpanel Displays and Devices 159 (2012).
[11] Thermal analysis of amorphous oxide thin-film transistor degraded by combination of joule heating and hot carrier effect, S Urakawa, S Tomai, Y Ueoka, H Yamazaki, M Kasami, K Yano, D Wang, M Furuta, M Horita, Y Ishikawa, Y Uraoka, Applied Physics Letters 102, 053506 (2013).
[12] Highly stable and textured hydrogenated ZnO thin films, S Y Myong, K S Lim, Applied Physics Letters 82, 3026 (2003).
[13] Impact of dopant species on the interfacial trap density and mobility in amorphous In-X-Zn-O solution-processed thin-film transistors, M Benwadih, J Chroboczek, G Ghibaudo,

R Coppard, D Vuillaume, Journal of Applied Physics 115, 214501 (2014).
[14] Working hypothesis to explore novel wide band gap electrically conducting amorphous oxides and examples, H Hosono, N Kikuchi, N Ueda, H Kawazoe, Journal of Non-Crystalline Solids 198–200, 165 (1996).
[15] High-mobility material research for thin-film transistor with amorphous thallium–zinc–tin oxide semiconductor, K Kishimoto, D-H Lee, I Kang, C-O Jeong, Y Ishikawa, H-S Kong, Japanese Journal of Applied Physics 54, 104101 (2015).

Chapter 3 First-principles simulation to estimate TlZnSnO TFT mobility

In this chapter, a first-principles simulation is conducted in order to estimate the TlZnSnO TFT mobility. First-principles simulation is a commonly used technique to estimate the effective masses of crystal Si semiconductor materials. Here, this approach is used to estimate the electron effective masses (m^*) of the InZnSnO (IZTO) and TlZnSnO oxide semiconductors with amorphous phase.

3.1 Experimental

3.1-1 First-principles simulation for amorphous phase in AOS

The first-principles calculations were performed using the projector augmented wave (PAW) method [1] of the Vienna ab-initio simulation package (VASP). [2] The Perdew–Burke–Ernzerh exchange–correlation functional (PBE) [3] approach utilizing the generalized gradient approximation (GGA) scheme was employed. The local density approximation with Hubbard parameter (LDA+U) method was employed to describe the localized semicore states of the Zn 3d orbitals. [4] These semicore orbitals are not accurately described by a normal LDA calculation, in which their overlap with the O p orbital is enhanced owing to a strong self-interaction effect in the localized orbital. However, it is

possible to compensate for the strong Coulomb energy at the localized d orbitals using the LDA+U method.

A simulated annealing (SA) process using molecular dynamic calculations on supercells was repeatedly employed in order to generate a reliable structure for the stoichiometric and O-deficient amorphous IZTO and TlZnSnO. The simulated temperature was increased to 4,000 K and then decreased slowly to 0 K. Then, the SA was repeated between 1,000 and 0 K, until the total energy and atomic structure converged conditionally. The performance of the TlZnSnO material was estimated by calculating its m^* via first-principles calculation. The relationship between m^* and the electron drift mobility (μ) is

$$\mu = q \times \tau / m^*, \text{ with } m^* \propto 1/(\partial E^2 / \partial K^2), \qquad (3.1)$$

where q is the charge, τ is the relaxation time, E is binding energy, and K is the wave number. Equation (3.1) indicates that high μ can be obtained with low m^*.

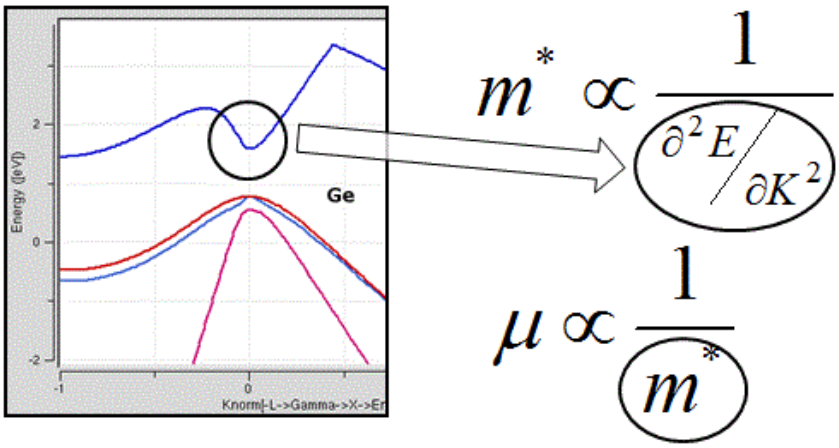

Fig. 3-1 Thematic diagram for mobility calculation from band structure and binding energy.

3.1-2 TlZnSnO supercells for first-principles simulation

In this study, binding energy of 5 eV was employed for the Zn 3d orbital only. The lattice constants of each of the binary oxides, ZnO, In_2O_3, SnO_2, and Tl_2O_3, which are 3.283, 10.16, 4.714, and 10.56 Å, respectively, were used. The author tested supercells containing 135 to 144 atoms, for materials with different compositions. Table 3-1 shows the different TlZnSnO compositions used in this simulation in terms of atom numbers. The Zn:Sn ratio was constant (3:2) to match the atomic composition of the ZTO target examined in chapter 2, and to remain close to the fundamental structure of the Zn_2SnO_4 crystal.

Table 3-1 Various TlZnSnO compositions (based on atom number) used in VASP simulation.

Ratio	# of atom				
Tl:(Sn+Zn) (Sn:Zn=2:3)	Tl	Sn	Zn	O	Total
1:9	6	20	30	79	135
2:8	12	18	27	81	138
3:7	18	16	24	83	141
4:6	24	14	21	85	144

3.2 Results and Discussion

3.2-1 Lattice structures of each TlZnSnO composition

ZnO is considered to provide the fundamental lattice structure of XZnSnO (X = Al, Ga, or In) and yields a wurtzite bonding structure. The atomic size of element X increases from the 1.18 Å of Al to the 1.44 Å of In with increasing atomic number, for group 3B of the periodic table. As the atomic sizes of both Al (1.18 Å) and Ga (1.26 Å) are smaller than that of Sn (1.40 Å), the largest s orbital size of Sn, which is related to the TFT mobility, is also reduced by increasing the Al and Ga content. This explains why Al and Ga do not dominate the increased TFT mobility in the ZnSnO structure. The atomic size of In (1.44 Å) is slightly larger than that of Sn (1.40 Å), and the In 5s orbital can be expected to contribute to the increased the TFT mobility of IZTO compared to that of ZnSnO. Based on this logic, the atom in group 3B that has the highest potential to increase the mobility for a ZnSnO structure is Tl, which has an atomic size of 1.48 Å and the 6s orbital. It is expected that the Tl 6s orbital will contribute to TlZnSnO having a higher TFT mobility than IZTO, even if both materials have the same Zn and Sn compositions.

The lattice structures of each composition in TlZnSnO after five repetitions of the SA process are shown in Fig. 3-2. A small number of changes were confirmed after five SA steps for each structure; thus, five SA steps were employed in the simulation. Of course, it is necessary to research the influence of various numbers of SA steps and the annealing

temperature in order to obtain more reliable results from this simulation. However, a very long period of time was required for the computer simulations involving all of the supercells with various compositions. Therefore, the only confirmation that was obtained was that the final structure cannot be fixed in a complex manner, even after more than five steps.

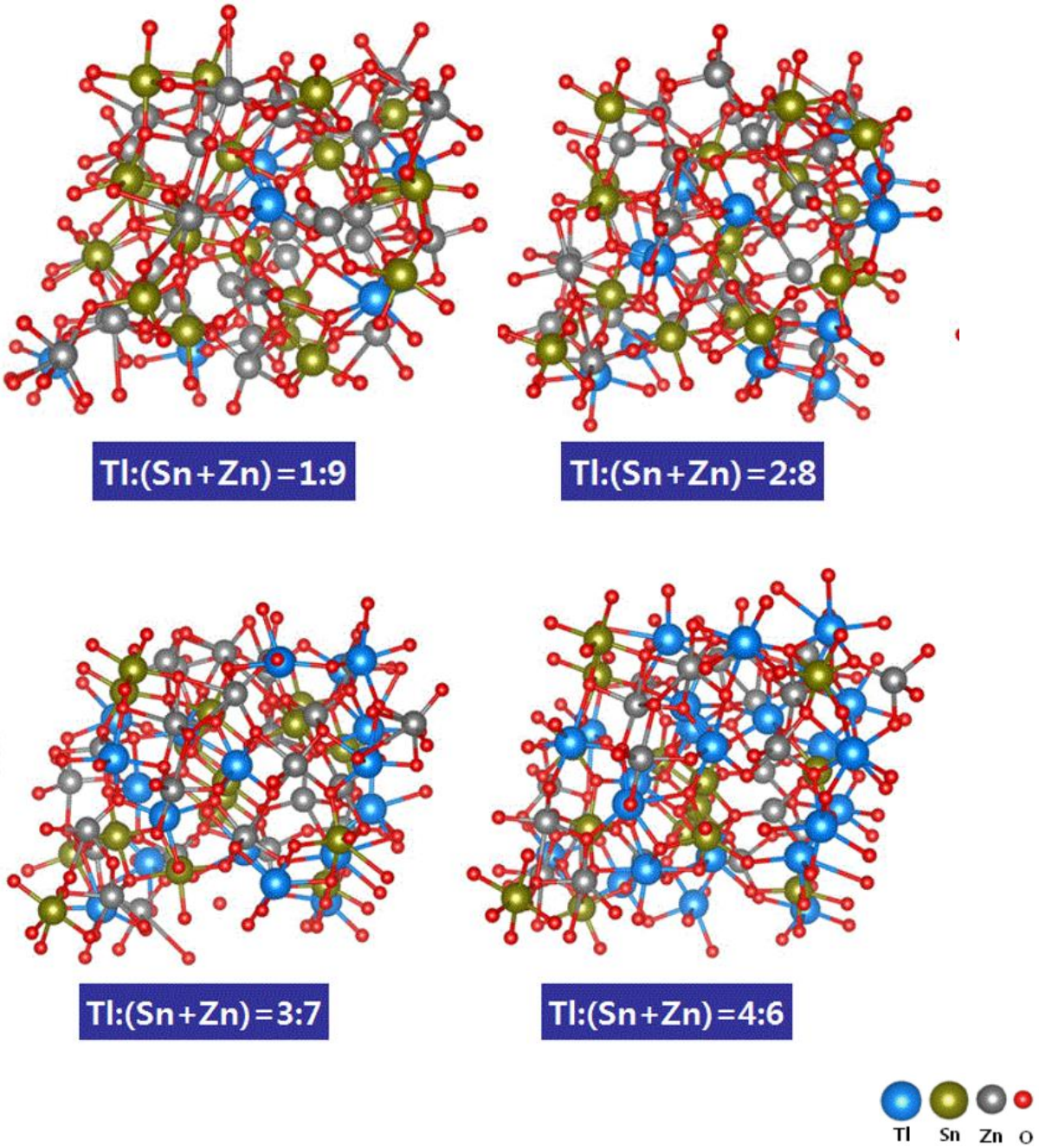

Fig. 3-2 Lattice structures of each examined TlZnSnO composition after five repetitions of SA process in VASP simulation.

In the case of the XZnSnO oxide compound, it is also known that it is difficult for the X element to form a crystal structure with Sn and Zn for Zn_2SnO_4, which constitutes a spinel structure compound. [5] Even if an X oxide crystal structure is likely to appear easily, the Zn_2SnO_4 prevents this because of the dissolution of X in that material. Accordingly, this characteristic makes it possible to increase the additive amount of X and reduce the electrical resistance. In addition, a good semiconductor thin film can be obtained without severe deposition condition requirements, such as high O partial pressure during film formation, through use of a sputtering target. Fig. 3-2 shows the conditions under which the Tl atoms are dissolved in Zn_2SnO_4, for Tl = 10, 20, 30, and 40 %. In the case of Tl = 10 and 20 %, higher dissolution of Tl in Zn_2SnO_4 is obtained, which yields high carrier density in the resultant films. On the other hand, for Tl = 30 and 40 %, a Tl-Tl bond appears, and it can be anticipated that the 6s orbitals of the Tl atoms have a strong influence on the electron mobility, yielding high mobility via percolation conduction.

3.2-2 Band structure according to Tl composition ratio in TlZnSnO

The author calculated and compared the m^* of IZTO and TlZnSnO with different In or Tl content values using first-principles simulation. As regards the characteristics of Tl oxide semiconductor materials, Kehoe et al. have previously reported the band structure and the total and partial electronic densities of states (PEDOSs) of Tl_2O_3, as calculated using the

Heyd-Scuseria-Ernzerhof exchange-correlation functional with standard parameter values (HSE06). [6] In their results, the main Tl 5d peak is separated from the bottom of the valence band, with small contributions from the Tl 6p, 5d, and 6s orbitals, and the bottom of the conduction band predominantly exhibits Tl 6s characteristics. The low conduction band minimum (CBM) position of the Tl-based oxide semiconductor materials makes a significant contribution to the reduced m^* and improves the material conductivity. On the other hand, the Tl-content dependence of the TlZnSnO energy bandgap is important for the semiconductor applications of that material. As the energy bandgap of Tl_2O_3 has been predicted to have a very small value of 0.33 eV, [6] TlZnSnO may also exhibit a small energy bandgap and acquire metallic characteristics with the addition of a large amount of Tl.

(a)

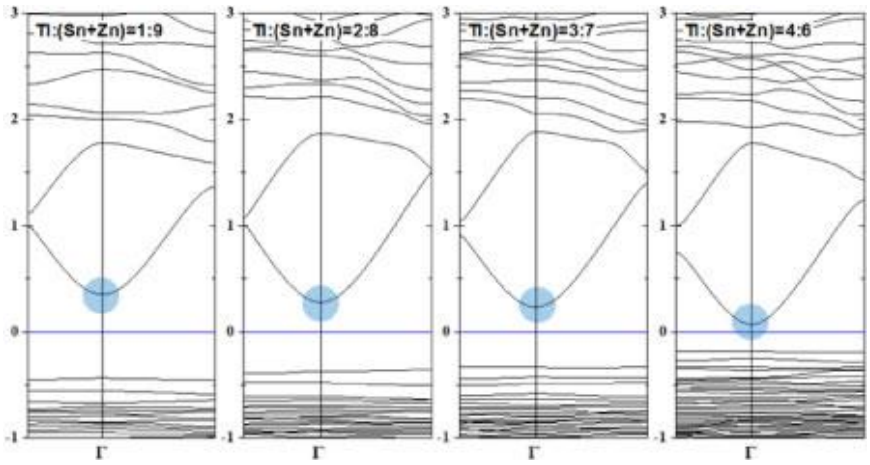

(b)

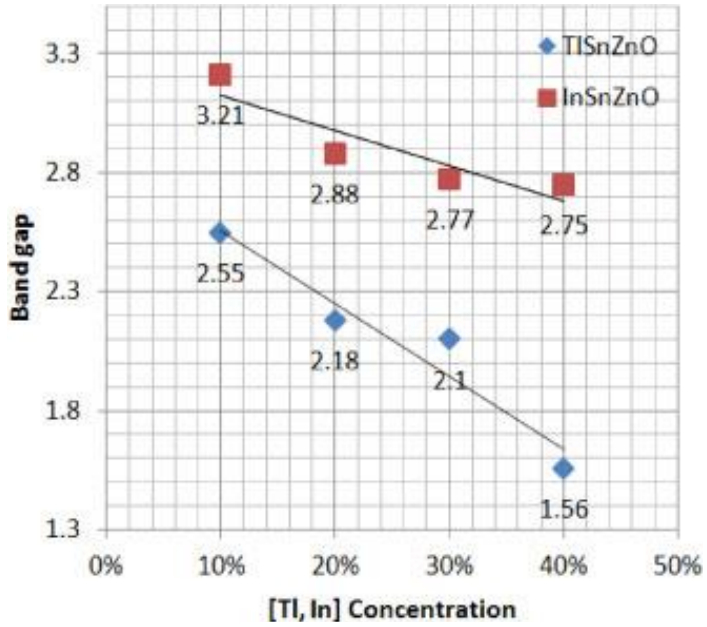

Fig. 3-3 (a) Band structures in accordance with Tl composition ratio of TlZnSnO, determined via first-principles simulation and (b) energy-band-gap dependence on XZnSnO composition; X = In (red squares) and Tl (blue diamonds).

3.2-3 Electron effective mass calculation for various X = Tl and In composition ratios in XZnSnO

Fig. 3-3 shows (a) the band structure and (b) the calculated energy bandgap in accordance with the Tl composition ratio in TlZnSnO, calculated using the HSE06 hybrid. The Zn/Sn composition ratio was held constant at 3/2 in this study, as discussed in relation to the $Zn_{0.6}Sn_{0.4}O$ (ZTO) composition in Chapter 2. In other words, although the Tl composition ratio was varied from 10 to 40 % for TlZnSnO, the Sn and Zn composition ratios remained constant under all conditions. The CBM positions indicated by the blue circles in Fig. 3-3 (a), which represent the 6s orbitals, grew closer to the Fermi level (E_F) with increased Tl content. This means that the Tl 6s orbital formed a shallow state near the CBM, and that m^* decreased with increased Tl composition. For IZTO, the In 5s orbital also formed a shallow state near the CBM and m^* also decreased with increased In composition. Moreover, the addition of Tl to ZnSnO had a stronger effect on decreasing the energy bandgap than the addition of In, as a result of the formation of a shallower 6s state near the CBM.

The energy bandgap decreased from 3.21 to 2.75 eV when the In composition was changed from 10 to 40 %, as shown by the red squares in Fig. 3-3 (b). As the Tl composition ratio was changed from 10 to 40 % in TlZnSnO, each bandgap also changed from 2.55 to 1.56 eV, as shown by the blue diamonds in Fig. 3-3 (b). Hence, it was confirmed that the TlZnSnO energy bandgap remained sufficiently large to maintain semiconductor characteristics, even

with a shallow state near the CBM. This indicates that TlZnSnO has high potential to act as a high-mobility semiconductor, similar to IZTO. The ZnSnO bandgap is 3.3 eV, [7] and our simulation data indicate a similar bandgap at the y-axis intersection (0 % Tl or In), which is consistent with our estimated bandgap. The optical bandgap for each composition ratio exhibits a strict dependence on the process conditions. Thus, it may be difficult to establish an actual relation between the composition and the bandgap.

Finally, the TlZnSnO mobility was estimated via a comparison of the m^* values of IZTO and TlZnSnO. The author compared the IZTO m^* for In composition ratios of 10–70 atom. %, with those of TlZnSnO for Tl composition ratios of 10, 20, 30, and 40 atom. %. The Tl and In composition ratio dependences of m^* in XZnSnO (X = Tl or In) are shown in Fig. 3-4. The light-green line and triangles indicate the m^* trend for TlZnSnO, whereas the red line and squares show that for IZTO. Several points were affected by changes in the quenched lattice structure during the temperature reduction from 1,000 K to 0 K of the SA process, for both TlZnSnO and IZTO. The ZnSnO m^* was speculated as being 0.290, considering the intersection between the y-axis and the IZTO trendline, because the IZTO line was less scattered than that of the TlZnSnO trend line, as a result of its wider bandgap and reduced interaction with the CBM. Based on the slopes of each trend line, m^* was reduced by more than three times by the addition of Tl to ZnSnO, compared to the reduction for added In (a ratio of 0.350/0.111). As regards the In composition of approximately 40 atom. % discussed

in Chapter 2, the author confirmed that the corresponding IZTO TFT mobility was more than 32.0 $cm^2(Vs)^{-1}$. The m^* of $Tl_{0.4}ZnSnO$ was simulated to be ~0.153, which is significantly smaller than that of $In_{0.4}ZnSnO$ (m^* = 0.243).

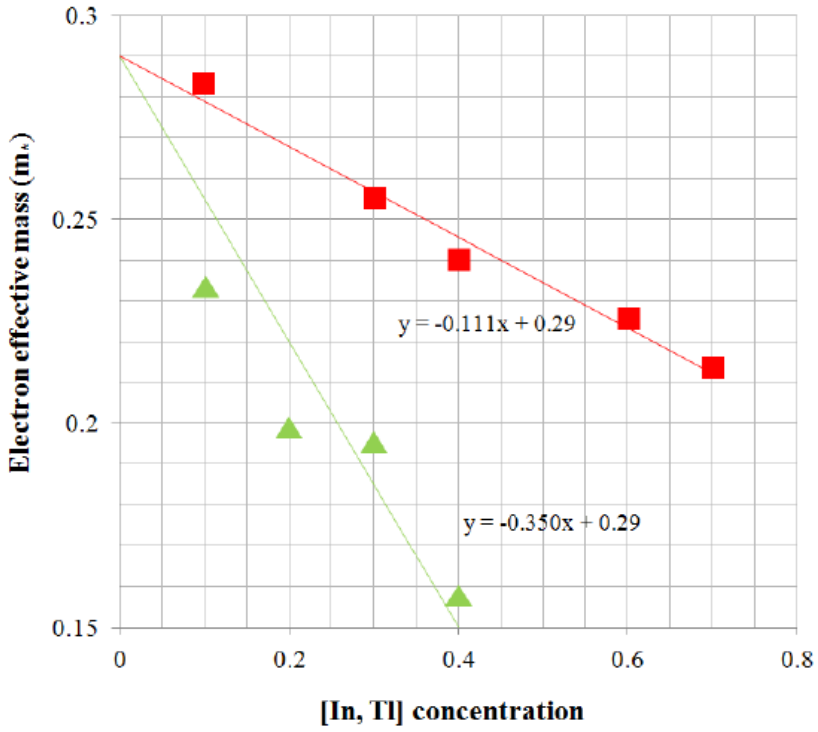

Fig. 3-4 Results of *m calculations for different Tl and In content values in XZnSnO (X = Tl or In). The light-green line and triangles indicate the TlZnSnO results, while the red line and squares show the IZTO data.**

Therefore, as m^* has an inverse relationship with the μ value, as shown in eq. (3.1), the $Tl_{0.4}ZnSnO$ TFT mobility is expected to be more than 50 $cm^2(Vs)^{-1}$. As shown in Fig. 3-3, the addition of Tl to ZnSnO materials is anticipated to contribute to reduced m^* and increased conductivity, as in the case of In_2O_3. [8] The relationship between the highest TFT mobility and the X s orbital size for XSnZnO (X = Al, Ga, In, or Tl) is shown in Fig. 3-5. The

TlZnSnO value was predicted based on first-principles simulation. The predicted TFT mobility of TlZnSnO is significantly higher than that of XSnZnO, where X = Al, Ga, or In. It is thought that this difference is related to the Tl-Tl bond that appears in the case of Tl = 30 and 40 %, and it can be anticipated that the 6s orbitals of the Tl atoms yield high electron mobility via percolation transportation, as shown in Fig. 3-1.

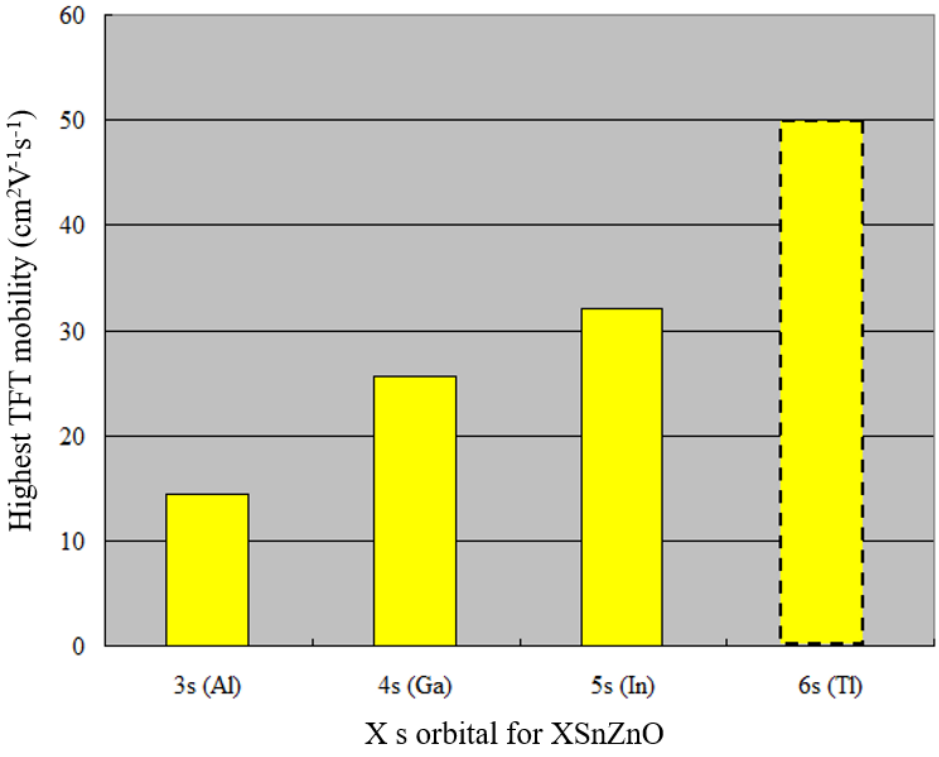

Fig.3-5 Relationship between highest TFT mobility and X s-orbital size for XSnZnO (X = Al, Ga, In, or Tl). The TlZnSnO value was predicted based on a first-principles simulation.

It should be noted that Tl-based oxide semiconductors should yield higher-stability and -reliability TFTs than In-based oxide semiconductors. Generally, the superior electrical stability of TFT materials with high field-effect mobility and high In content is extremely

difficult to maintain, because of the unstable Vo. [9] However, the electrical stability and reliability of TlZnSnO has not yet been investigated. Thus, it is meaningful to discuss the properties and stability of each relevant binary metal-oxide material, in order to determine the electrical stability of the unknown multi-component material, TlZnSnO. The electrical properties of TlZnSnO and IZTO have already been compared. Next, we focus on the stability of the Vo defects between In_2O_3 and Tl_2O_3, in terms of the shallow donor state creation and with regard to the film stability, in order to examine the reliabilities of both IZTO and TlZnSnO.

In the case of In-oxide materials, Limpijumnong et al. have reported the formation energies of the Vo defects, interstitial hydrogen (Hi), and substitutional hydrogen (H_O) under In-rich/O-poor conditions. [9] Through the addition of Hi, H substitution on the O site appears, with the H_O combination acting exclusively as a donor. It is easy for H diffusion to change the CBM position by increasing the number of donors. At that time, as the Vo transition point from Vo^0 to Vo^{2+} is very close to the In_2O_3 bandgap at 2.67 eV, the Vo defects easily change between Vo^0 and Vo^{2+} through slight shifting of the CBM level. This is one of the main reasons why In-based oxide semiconductors are unstable and have low reliability. Kehoe et al. have calculated the formation energies of Vo defects under both Tl-rich/O-poor and Tl-poor/O-rich conditions. [6] In the case of Tl-oxide materials, the CBM position is extremely low and separated from the transition point between Vo^{2+}, Vo^{+}, and Vo^0 under both

sets of examined conditions. Thus, it is difficult to change the Vo defect charge through movement of the CBM in the case of a Tl-based oxide semiconductor. Therefore, it is expected that Tl-based oxide semiconductors will exhibit superior TFT stability to In-based oxide semiconductors.

3-3. Conclusion

In this chapter, the potential TlZnSnO TFT performance was examined via a first-principles simulation, in which the m^* of IZTO and TlZnSnO were estimated. The results suggest that $Tl_{0.4}ZnSnO$ has a mobility of more than 50 $cm^2V^{-1}s^{-1}$ owing to the emergence of the 6s orbital of Tl. This is higher than that of $In_{0.4}ZnSnO$, which has a mobility of 32.0 $cm^2V^{-1}\ s^{-1}$ for the same Zn and Sn content. The source of this improvement is thought to be the Tl-Tl bond that appears in the case of Tl = 30 and 40 %, and it can be anticipated that the 6s orbital of the Tl atoms has a strong influence on the electron mobility, based on the percolation transportation model.

References:

[1] Projector augmented-wave method, P E Blöchl, Physical Review B 50, 17953 (1994).
[2] Efficient iterative schemes for ab initio total-energy calculations using a plane-wave basis set, G Kresse, J Furthmüller, Physical Review B 54, 11169 (1996).
[3] Generalized gradient approximation made simple, J P Perdew, K Burke, M Ernzerhof, Physical Review Letters 77, 3865 (1996).
[4] Band theory and Mott insulators: Hubbard U instead of Stoner I, V I Anisimov, J Zaanen, O K Andersen, Physical Review B 44, 943 (1991).
[5] A simple method to synthesize single-crystalline Zn2SnO4 (ZTO) nanowires and their photoluminescence properties, S Wang, X Zhang, X Liao, W Yang, Nanotechnology 16, 2928 (2005)
[6] Nature of the band gap of Tl_2O_3, A B Kehoe, D O Scanlon, G W Watson, Physical Review B 83, 233202 (2011).
[7] Origin of the improved mobility and photo-bias stability in a double-channel metal oxide transistor, H Y Jung, Y Kang, A Y Hwang, C K Lee, S Han, D-H Kim, J-U Bae, W-S Shin, J K Jeong, Scientific Reports 4, 3765 (2014).
[8] Band gap engineering of In_2O_3 by alloying with Tl_2O_3, D O Scanlon, A Regoutz, R G Egdell, D J Morgan, G W Watson, Applied Physics Letters 103, 262108 (2013).
[9] Hydrogen doping in indium oxide: An ab initio study, S Limpijumnong, P Reunchan, A Janotti, C G van de Walle, Physical Review B 80, 193202 (2009).

Chapter 4 Reactivity and stability of Tl_2O_3 for TlZnSnO fabrication

Tl-related materials have not been widely produced on account of their toxicity and high reactivity. In particular, it is well-known that sulfide-based Tl alloys can be absorbed by and accumulate in the human body. [1] On the other hand, Tl oxides are rather stable and safe for use in semiconductor research and production. [2, 3] In this chapter, the stability of Tl oxide materials is examined, with a view to fabricating a TlZnSnO powder for a sputtering target. First, we investigate the reactivity of Tl_2O_3 with ZnO, SnO_2, and In_2O_3 in order to establish a reaction route for TlZnSnO. Then, TlZnSnO powder is prepared based on the results of the reactivity experiments.

4.1 Experimental

The raw materials, namely, ZnO (99.99 %), SnO_2 (99.99 %), In_2O_3 (99.99 %), and Tl_2O_3 (99.9 %) powders, were provided by Kojundo Chemical Laboratory Co., Ltd. The particle size was approximately 1 μm for all powders. First, we investigated the reactivities for the binary oxide systems. The fabrication flow chart is shown in Fig. 4-1 (a), in which the

specimens comprised of Tl_2O_3 powder mixed with ZnO, SnO_2, and In_2O_3 are labeled TZO, TTO, and TIO, respectively. The cation molar ratio Tl/M (M = Zn, Sn, and In) was fixed to 0.5. Binary powder specimens with a total weight of 2 grams were mixed using an agate mortar and pestle, and then pressed into pellets with 10-mm diameter and 1–2-mm thickness under a pressure of 20 MPa. Each pellet was sealed in a quartz ampoule under an air atmosphere of 0.03 MPa. The ampoule was then heated to 600 ºC and this temperature was maintained for 18 h. Note that fabrication of a $Tl_{0.8}Sn_{0.2}$ compound from metal Tl and Sn at temperatures of more than 273 ºC was expected, as shown in Fig. 4-2. Further, it was thought that the Tl reaction could be suppressed by the 18-h calcination at 600 °C.

After calcination, each specimen was analyzed using X-ray diffraction (XRD; X'Pert Pro, PANalytical) for phase identification, X-ray photoelectron spectroscopy (XPS; PHI5000 VersaProbeII, ULVAC-PHI) to investigate the reactivity produced by chemical shifting of the elements, and scanning electron microscopy (SEM) with energy dispersive X-ray spectroscopy (EDX). In the EDX measurement, the acceleration voltage was 7 kV. Thus, the signals were obtained from a particle depth of less than 1 micron, indicating that the surface reaction of each particle was primarily observed (recall that the particle sizes were approximately 1 μm).

Two routes were employed to fabricate the TlZnSnO powder, as shown in Fig. 4-1 (b). The Tl_2O_3, ZnO, and SnO_2 mixed powders were used as starting materials for a component labeled

TZTO-01. For the other component, labeled TZTO-02, Tl_2O_3 and pre-prepared ZnSnO powders were used. The ZnSnO powders were obtained through calcination of ZnO and SnO_2 powders at 1000 ºC for 24 h under atmosphere. The cation composition was controlled to 10.7 at.% Tl, 35.7 at.% Zn, and 53.6 at.% Sn. During the pellet forming, the heat treatment and analyses were conducted in the same manner as for binary powders.

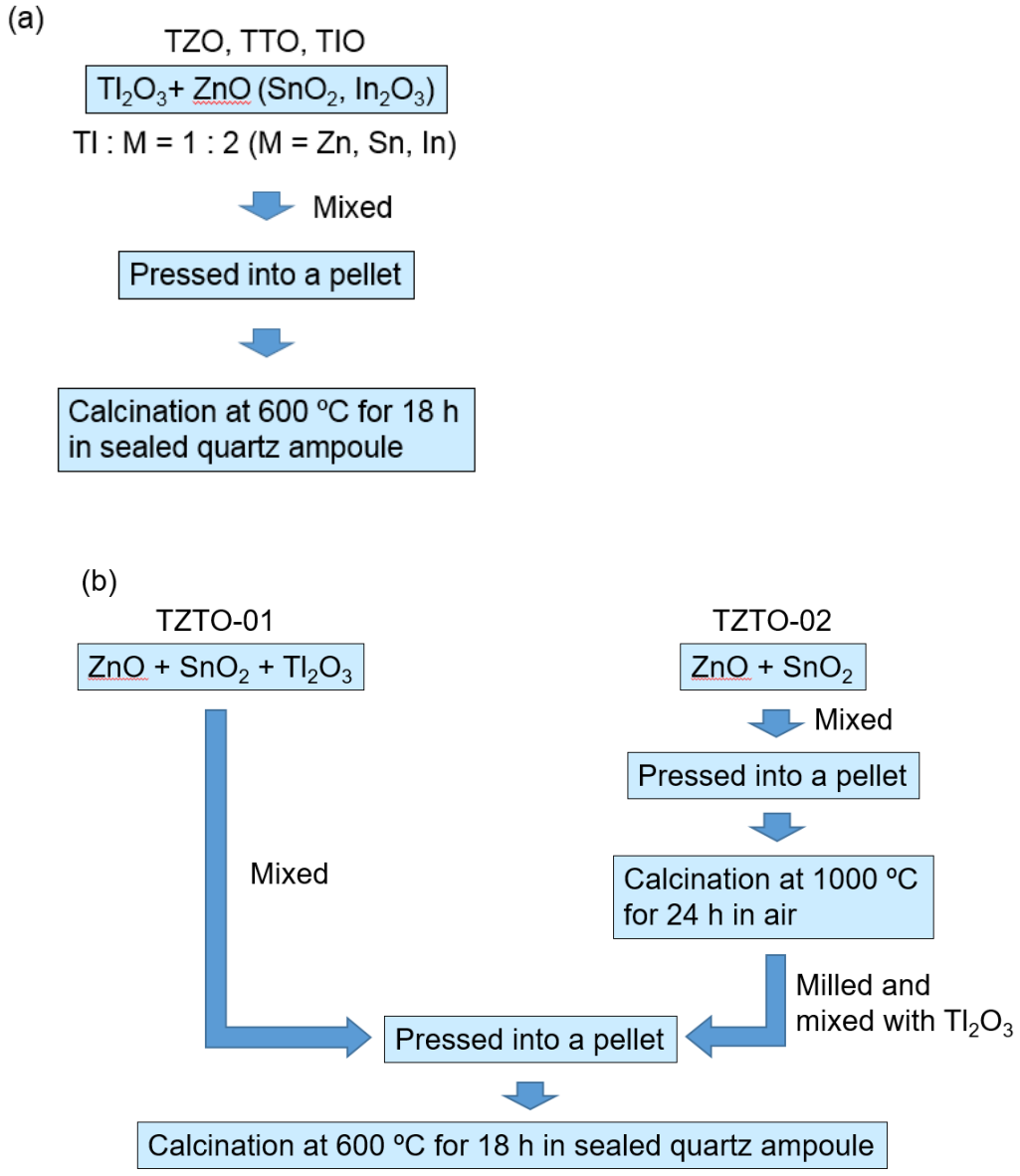

Fig. 4-1. (a) TZO, TTO, TIO, and (b) TlZnSnO fabrication processes.

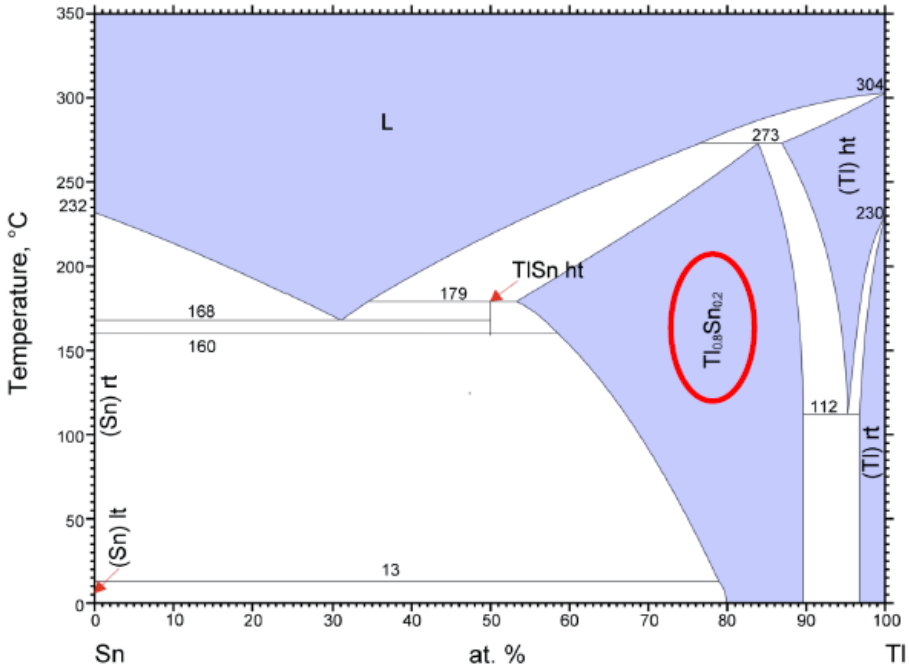

Fig.4-2. Phase diagram for Sn-Tl metals.

4.2 Results and discussion

4.2-1. Reaction in binary oxide system

Figure 4-3 shows the XRD profiles of the binary powder specimens before and after calcination. In each specimen, other materials such as complex oxides remained unidentified after calcination. As a result of the calcination, the intensities of the Tl_2O_3 peaks decreased relative to those attributed to the ZnO, SnO_2, and In_2O_3, with the specific decreases differing among the specimens. Consequently, the difference in the peak intensity ratio, I_{Tl2O3}/I_{MO} (where I_{Tl2O3} and I_{MO} indicate the Tl_2O_3 and metal-oxide peak intensities, respectively), before and after calcination was investigated for each specimen. In the evaluation, the (222) diffraction peaks were considered for Tl_2O_3 and In_2O_3. For ZnO and SnO_2, the (101) and (110) diffraction peaks were used, respectively.

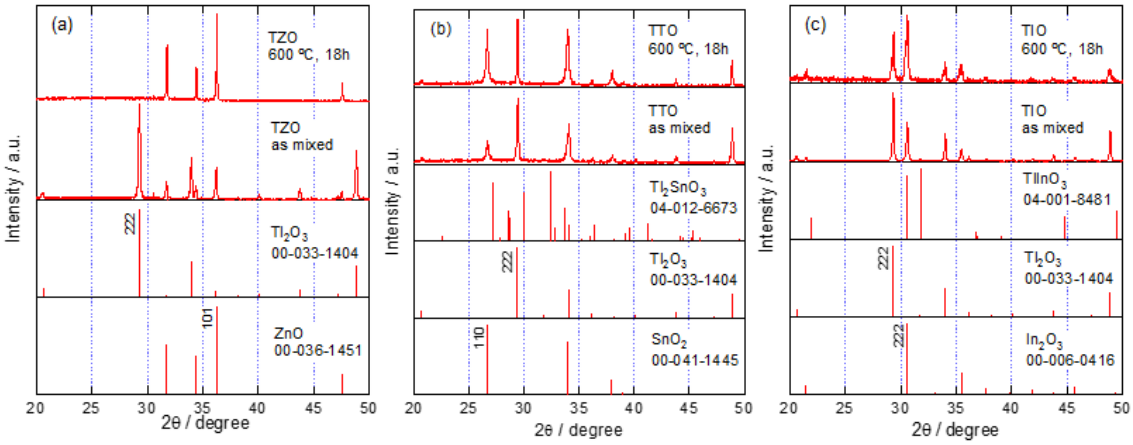

Fig. 4-3. XRD profiles of (a) TZO, (b) TTO, and (c) TIO before and after calcination.

The I_{Tl2O3}/I_{MO} results obtained from the TZO, TTO, and TIO XRD profiles are summarized in Table 4-1. The differences between the ratios before and after calcination are also shown. For all specimens, I_{Tl2O3}/I_{MO} decreased after calcination, which indicates that Tl_2O_3 reacts with the oxides. However, the magnitudes of the differences vary largely among the specimens, which may indicate reactivity in the binary system. That is, Tl_2O_3 is more reactive with ZnO.

Table 4-1 XRD profile peak intensity ratios of TZO, TTO, and TIO.

Specimen	Ratio of peak intensity, I_{Tl2O3} / I_{MO}		
	(*A*) as mixed	(*B*) after calcination	
TZO	2.97	0	1
TTO	2.81	1.19	0.57
TIO	1.76	0.75	0.57

Figure 4-4 shows SEM images and elemental mappings of TZO, TTO, and TIO after calcination at 600°C for 18 h. The TZO particles have clear spherical shapes, as can be seen in Fig. 4-4 (a). On the other hand, the TTO and TIO particles are finer and irregularly shaped, as shown in Figs. 4-4 (b) and (c). Some particles are approximately 1 μm in size, the same as those of the raw materials, although particles with smaller diameters can also be observed. The Tl mappings differ among the samples. Specifically, the Tl was unevaporated and uniformly distributed on the ZnO particles in the TZO specimen. On the other hand, Tl was observed in localized distributions in the case of TTO and TIO.

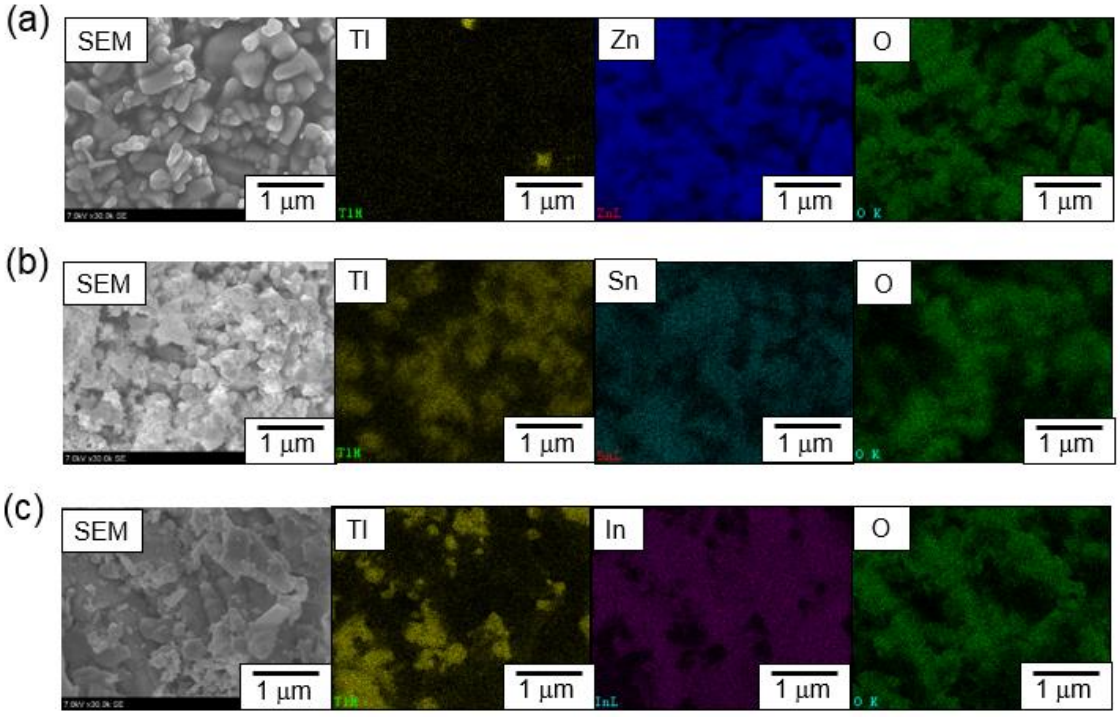

Fig. 4-4. SEM images and elemental mappings of (a) TZO, (b) TTO, and (c) TIO after calcination.

4.2-2. XPS profiles of Tl 4f and O 1s in binary system before and after calcination

The XPS profiles of Tl 4f and O 1s in TZO are shown in Fig. 4-5. Two peaks are apparent in Fig. 4-5 (a), which were identified as the spin-orbit splittings, $4f_{7/2}$ and $4f_{5/2}$. The binding energies for $4f_{7/2}$ and $4f_{5/2}$ in Tl_2O_3 are approximately 117 and 122 eV, respectively [13], and the binding energies observed in the as-mixed TZO were 116.5 and 121 eV, respectively. The latter values are thought to be influenced by the presence of Tl_2O_3. After calcination, the Tl 4f

binding energies shifted to higher values, i.e., 118 and 123 eV, respectively, which implied that the Tl stability increased through reaction with ZnO. The O 1s profile for the as-mixed specimen shown in Fig. 4-5 (b) is complex, and it is understood that the shape was altered by the reaction caused by the calcination.

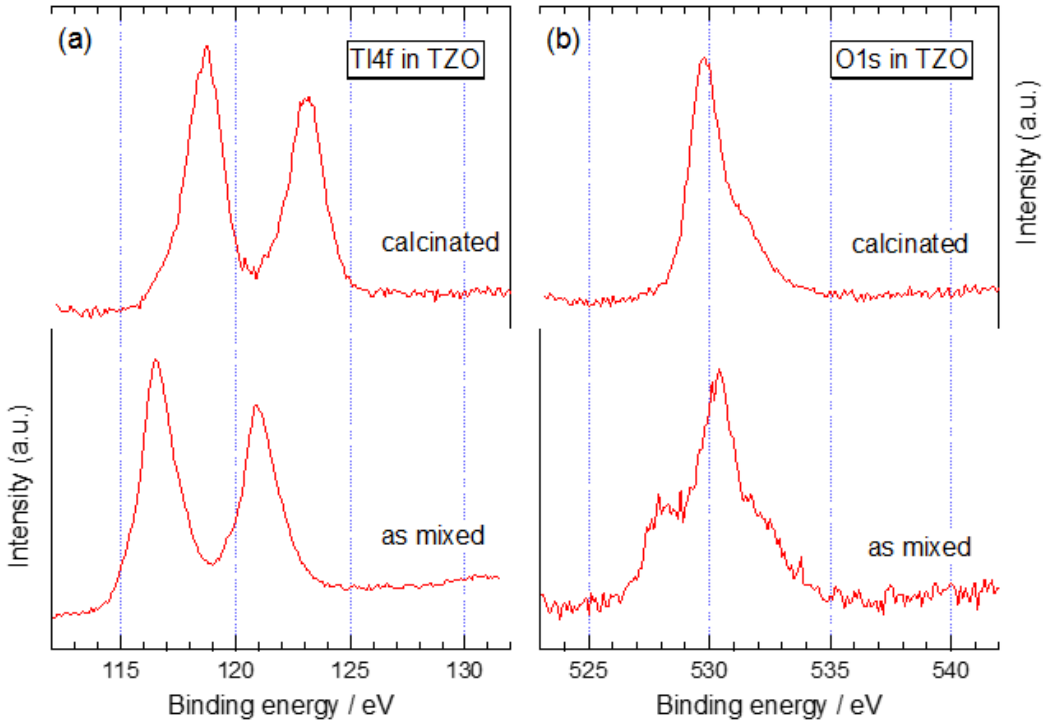

Fig. 4-5. XPS profiles of (a) Tl 4f and (b) O 1s in TZO before and after calcination.

The profiles of the as-mixed specimens seem to consist of three peaks, which have center positions at 528.5, 530, and 532 eV. Consequently, peak deconvolution was conducted using Gaussian functions and the area intensities of each resolved spectrum before and after calcination were compared, in order to evaluate the reactivity. The area intensities of the Tl $4f_{7/2}$ spectra were also analyzed. Fig. 4-6 shows the area intensity ratios for the analyzed spectra before and after calcination. This analysis was also conducted for TTO and TIO.

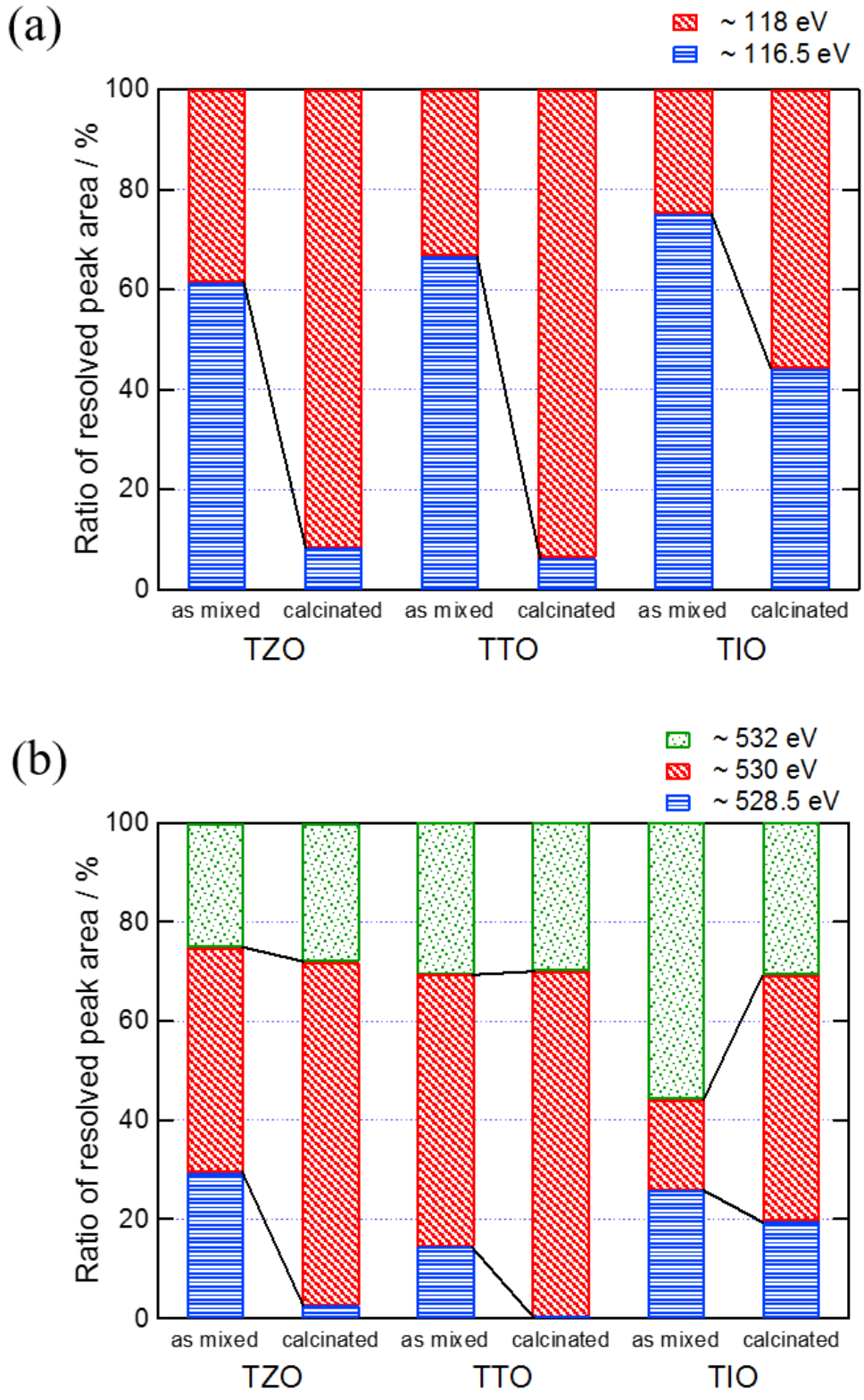

Fig. 4-6. Fractions of resolved peak areas for (a) Tl $4f_{7/2}$ and (b) O 1s in TZO, TTO, and TIO, before and after calcination.

Two resolved peaks can be obtained for the Tl $4f_{7/2}$ profiles of any specimen. The area intensity of each spectrum at lower energy decreases after calcination. It is understood that reactions occur between the oxides. In particular, the fractions of the spectra at lower binding energies are below 10% after calcination in the case of both TZO and TTO, which indicates that ZnO and SnO_2 with Tl_2O_3 are more reactive than In_2O_3 with Tl_2O_3. In the O 1s profiles, three peaks can be identified. Further, the fractions of the spectra at the lowest energies decrease and those at the intermediate energies increase after calcination. A remarkable change is apparent for TZO and TTO. Comparing the TZO O 1s XPS profiles with those of the ZnO and Tl_2O_3 reagents (Fig. 4-7), the spectrum data at the lowest binding energy is from Tl_2O_3. Therefore, the decrease in the area fraction of the spectrum at the lowest energy indicates the reaction of Tl_2O_3 with ZnO, SnO_2, or In_2O_3 as a result of calcination at 600 ºC. This coincides with the Tl 4f results.

The reactivity of SnO_2 is similar to that of In_2O_3, according to the XRD results shown in Fig. 4-3 and Table 4-1. The XPS profiles, however, indicate that SnO_2 is more reactive. It is thought that the difference between the XRD and XPS trends is due to the Tl_2O_3 surface reaction with the ZnO, SnO_2, and In_2O_3 particles during calcination. As regards calcination with ZnO, the partial pressure of the Tl_2O_3 atmosphere decreases sufficiently for vaporization of Tl_2O_3 to occur, because of the considerably higher reactivity of Tl on ZnO. Hence, the Tl_2O_3 particles vaporize and the XRD peak degrades completely. It can be understood that the

TZO particles have clearly spherical shapes, as shown in Fig. 4-4(a). This coincides with the XPS results.

On the other hand, in the case of calcination with SnO_2 or In_2O_3, the partial pressure of the Tl_2O_3 atmosphere does not vary significantly, because of the decreased reactivity of Tl on SnO_2 or In_2O_3. Hence, the Tl_2O_3 particles do not vaporize completely and remain part of the TTO or TIO particles, through the surface reactivity reduction caused by the attachment of the non-reactive Tl_2O_3 to the SnO_2 or In_2O_3. Both particles with sizes of approximately 1 μm and smaller particles, which seem to be non-reactive Tl_2O_3, were observed, as shown in Fig. 4-4 (b) and (c). The XPS results indicate that Tl_2O_3 has higher reactivity on an SnO_2 particle than on an In_2O_3 particle. In addition, the increased reactivity of Tl_2O_3 on SnO_2 is sufficient to prevent retention of a clear SnO_2 particle surface. Thus, it is concluded that the low-to-high reactivity order with Tl_2O_3 is ZnO, SnO_2, and In_2O_3.

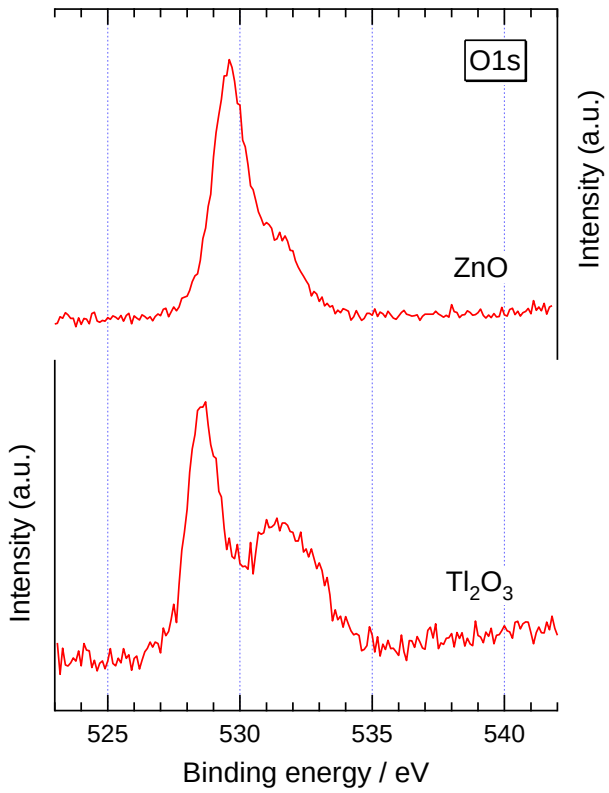

Fig. 4-7. XPS profiles of O 1s in ZnO and Tl_2O_3.

4.2-3 Fabrication of TlZnSnO

Based on the results of the binary oxide system analysis, we prepared ZnO-SnO_2-Tl_2O_3 system specimens in order to fabricate TlZnSnO. To fabricate a TlZnSnO tablet, the two routes shown in Fig. 4-2 (b) were employed. Thus, mixed powders comprised of Tl_2O_3, ZnO, and SnO_2 were used as starting materials for TZTO-01. The second component, TZTO-02, was comprised of Tl_2O_3 and pre-prepared ZnSnO powders. The ZnSnO powders were obtained via calcination of ZnO and SnO_2 at 1000 ºC for 24 h under atmosphere. The cation composition was controlled to 10.7 at.% Tl, 35.7 at.% Zn, and 53.6 at.% Sn. The pellet

forming, heat treatment, and analyses were conducted in the same manner as for the binary powders.

Note that ZTO is a spinel chemical compound. [5] Spinels are members of a class of minerals of general formulation $A^{2+}B^{3+}{}_2O^{2-}{}_4$, which crystallize in the cubic (isometric) crystal system, with the oxide anions arranged in a cubic close-packed lattice and the cations A and B occupying some or all of the octahedral and tetrahedral sites in the lattice. [6] Fig. 4-8 shows one example of a spinel structure. Normal spinel structures are usually cubic close-packed oxides with two octahedral and one tetrahedral sites per formula unit. The tetrahedral spaces are smaller than the octahedral spaces. B^{3+} ions occupy half the octahedral holes, while A^{2+} ions occupy one-eighth of the tetrahedral holes.

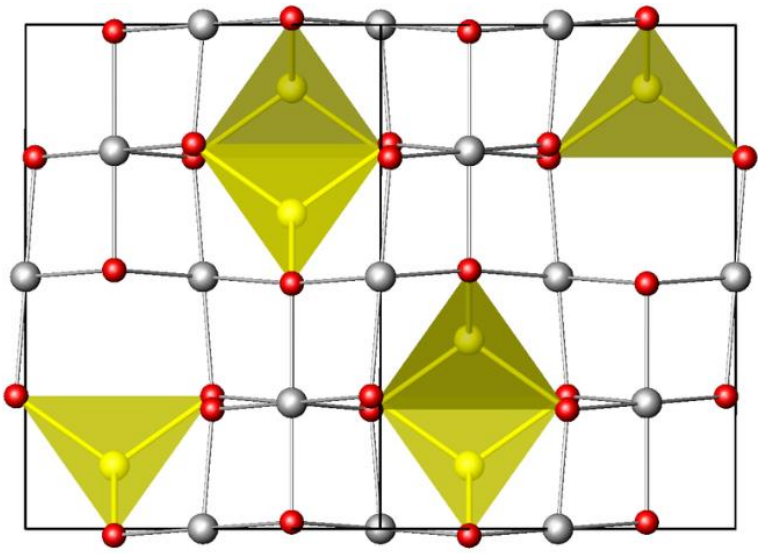

Fig. 4-8. Example of spinel structure [6].

The ZTO crystal is expected to contribute two beneficial properties to the sputtering

process. First, in the case of oxide target preparation for reactive sputtering, a low electrical resistance is especially important to prevent abnormal discharge by the partially ionized arc plasma on the target. The crystallinity of a semiconductor material such as ZTO fundamentally reduces the resistance [7]. In addition, similar to InSnZnO (in which In is dissolved in ZTO), ZTO has high mobility and high carrier concentration [8]. Through its increased mobility and carrier concentration, the ZTO can significantly reduce the resistance when the solid solubility of the Tl is increased. Second, as the thermal conductivity of the target is increased by the higher density induced during crystallization, the ZTO crystal prevents increases to the target temperature during sputtering, which can suppress target cracking [9].

In this experiment, the author determined the XRD profiles of both the TZTO-01 and TZTO-02 samples after calcination at 600 °C for 18 h, as shown in Fig. 4-9. Here, XRD patterns for both as-mixed and annealed samples are shown. Further, the XRD patterns of ZnO (card number: 00-036-1451), SnO_2 (card number: 00-041-1445), and Tl_2O_3 (card number: 00-033-1404) are also presented for reference. The XRD results for the as-mixed and annealed samples were compared in order to confirm the volume change of the ZnO, SnO_2, and Tl_2O_3 crystals after the annealing process, which can be determined through comparison of the Tl (222) peak with the Zn (101) or Sn (110) peaks. For the TZTO-01 powder, the ZnO and SnO_2 peaks remained almost unchanged, even after calcination. In contrast, the

Tl_2O_3-related peaks almost disappeared after calcination. Further, no new peaks appeared after the calcination at 600 °C for 18 h. Thus, no other crystal was generated via calcination for the TZTO-01 samples, which conforms to the results shown in Fig. 4-3. On the other hand, for the as-mixed TZTO-02 sample, the Tl_2O_3-related peaks disappeared almost completely after calcination. However, the ZTO crystal peak was clearly apparent. This peak remained after calcination with Tl_2O_3.

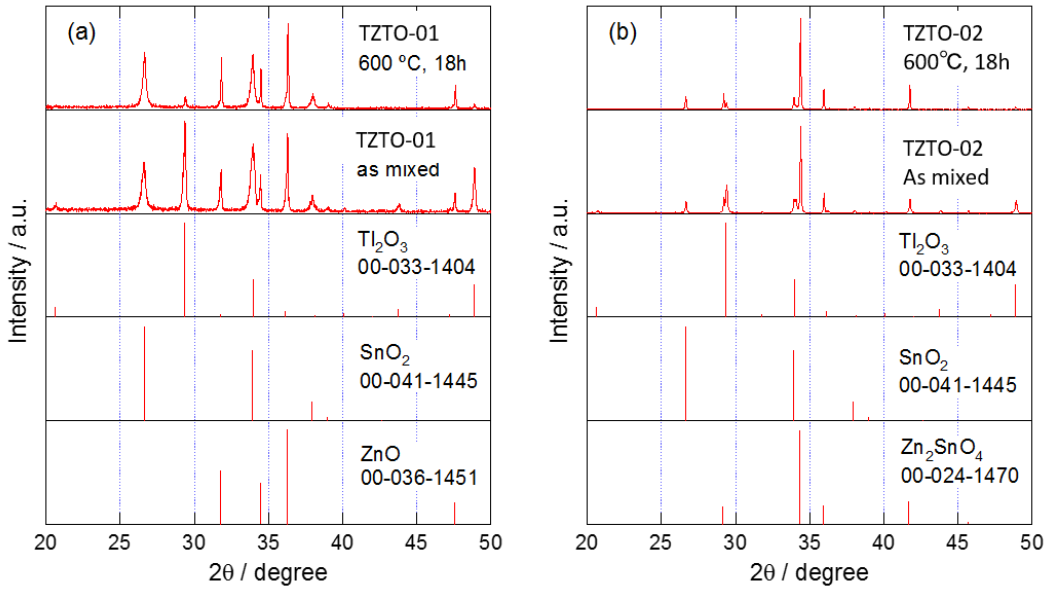

Fig. 4-9. XRD profiles of (a) TZTO-01 and (b) TZTO-02 before and after calcination.

4.2-4. XPS profiles of Tl 4f and O 1s in TlZnSnO before and after calcination

Figure 4-10 displays the bonding ratios related to (a) Tl 4f and (b) O1s estimated from the XPS spectra for both the as-mixed and annealed (600 °C, 18 h) TZTO-01 and TZTO-02 samples. The Tl 4f peak was separated into two peaks centered at 116.5 and 118 eV, as in the results shown in Fig. 4-5 (a). The 116.5-eV bonding ratio decreased in the vicinity of the half volume, and the stronger bonding of 118 eV became the main phase. For the TZTO-01 and TZTO-02 powders, the weaker bonding remained at approximately 35 % and 40 % of the original values, respectively, even after calcination. This result shows that the reactions between Tl and SnO_2 or ZnO in the TZTO-01 compound were suppressed compared with the expected reaction, which was observed in the TZTO-02 and SnO_2+Tl_2O_3 cases, where the weaker (116.5 eV) bonding ratio was less than 10 % after calcination, as shown in Fig. 4-5.

On the other hand, in the case of O 1s, the behavior of the peaks centered at 532 eV and 530 eV differed slightly for each material. The peak centered at 528 eV for the as-mixed powders was almost completely diminished following calcination, for all specimens. In the case of TZTO-01, the bonding ratio of the peak centered at 532 eV changed from 35 % to approximately 45 % following calcination, which suggests that the 10 % ratio of the weaker bonding state (530 eV) became an intermediate higher-energy bonding phase. On the other hand, in the case of TZTO-02, the ratio of the peak centered at 532 eV reduced to 27 % after

ZTO fabrication and then changed to approximately 52 %, which suggests that the 25 % ratio of the 530-eV weaker bonding state was changed to an intermediate higher-energy bonding phase by the calcination. Hence, it is clear that ZTO has identical or greater reactivity with Tl_2O_3 than the SnO_2 and ZnO mixed particles, despite the more stable dispersion of the Zn and Sn atoms. Higher-stability TZTO can be fabricated from the TZTO-02 powder using suitable thermal processes, and it is expected that a superior TZTO sputtering target with low resistance and high density can be obtained as a result.

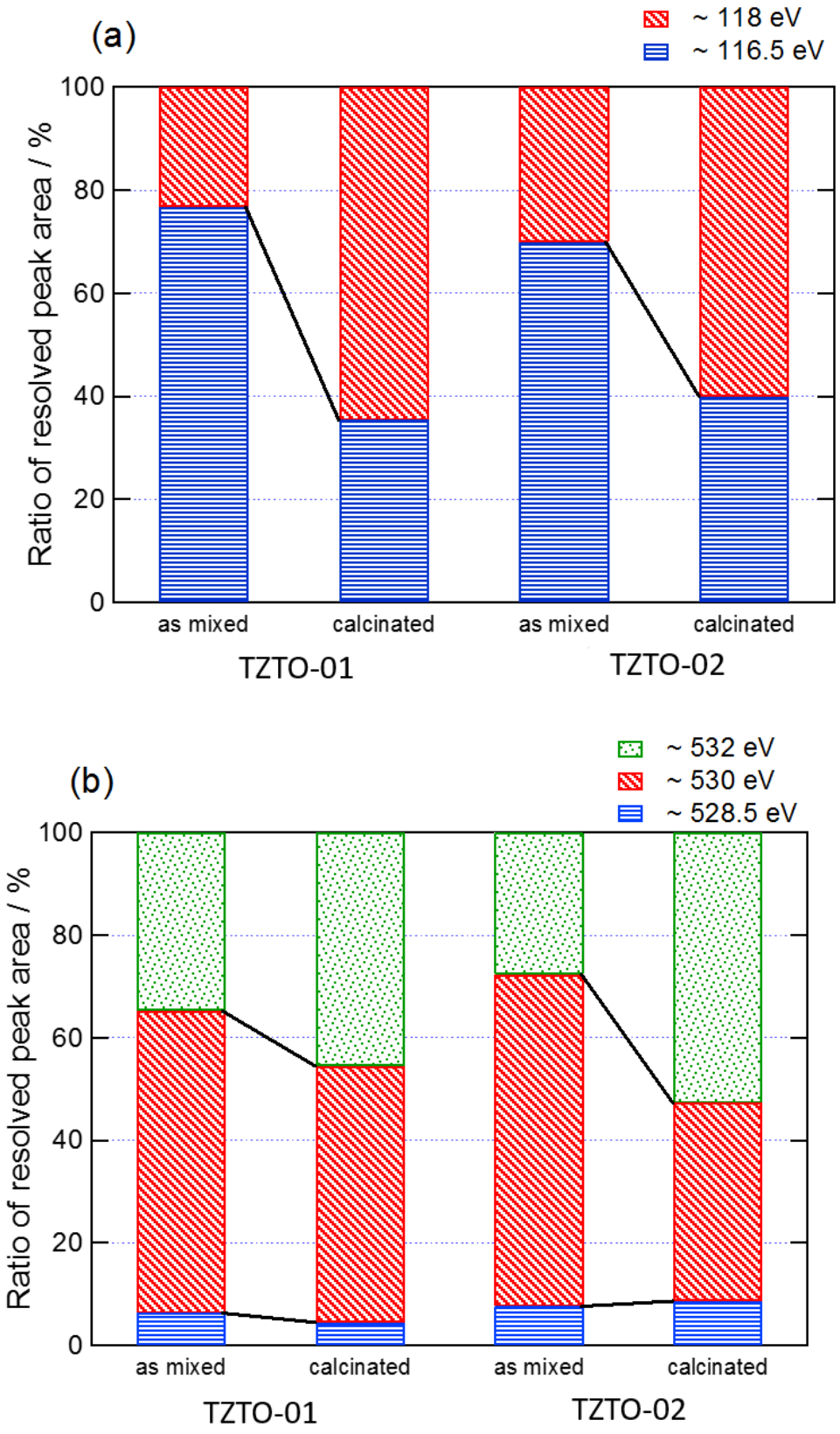

Fig. 4-10. Fraction of resolved peak area for (a) Tl $4f_{7/2}$ and (b) O 1s in TZTO-01 and TZTO-02, before and after calcination.

4-3. Conclusion

The thermal reactions between Tl_2O_3 and ZnO, SnO_2, or In_2O_3 induced by annealing at 600 °C for 18 h in an air atmosphere were investigated. From the XRD results for the annealed samples, Tl_2O_3 had the greatest reactivity with ZnO. EDX analysis indicated the mechanism through which the Tl atoms scatter and attach uniformly to the ZnO particles only. XPS data was also analyzed in order to compare the O 1s and Tl 4f bonds of the as-mixed samples with those of annealed samples. Hence, it was found that Zn and Sn can contribute to improvements in the Tl and O bonding stability; however, the affinity of In for Tl is weaker than that of Zn or Sn. Finally, the author prepared three- (TZTO-01 powder) and two-element-mixed samples (TZTO-02 powder), which were annealed at 600 °C for 18 h. Hence, it was clarified that ZTO has identical or greater reactivity with Tl_2O_3 than SnO_2 and ZnO mixed particles, despite the higher stability and sufficient dispersion of the Zn and Sn atoms. Higher-stability TlZnSnO can be fabricated from TZTO-02 powder via suitable thermal processes. It is expected that a TlZnSnO sputtering target can be fabricated through suitable calcination.

References

[1] Thermodynamic properties of liquid silver--thallium alloys, K Kameda, Y Yoshida, S Sakairi, Journal of the Japan Institute of Metals and Materials 47(5), 406 (1983).
[2] Efficient thallium photodissociation laser, D J Ehrlich, J Maya, R M Osgood Jr., Applied Physics Letters 33, 931 (1978).
[3] Gain in a thallium iodide laser with external resonator, P Burkhard, W Lüthy, T Gerber, Optics Letters, **5**(12), 522 (1980).
[4] G E Muienberg, Handbook of X-ray Photoelectron Spectroscopy, Perkin-Elmer Corporation (1979).
[5] Transparent conducting oxides in the ZnO-In_2O_3-SnO_2 system, A J Freeman, K R Poeppelmeier, T O Mason, R P H Chang, T J Marks, MRS Bulletin, Volume 25, Issue 08, 45 (2000).
[6] http://nptel.ac.in/courses/113104005/lecture3/3_9.htm
[7] Reducing resistance of polycrystalline layer by doping, heating, and applying radiation beam, T Shibata, Method for manufacturing a semiconductor device, US4309224 A (1982).
[8] High-mobility material research for thin-film transistor with amorphous thallium–zinc–tin oxide semiconductor, K Kishimoto et al., Japanese Journal of Applied Physics 54, 104101 (2015)
[9] Novel manufacturing design and processing methods and apparatus for sputtering targets, J. Kardokus, Novel Manufacturing Design and Processing Methods and Apparatus for Sputtering Targets, 20080289958 A1 (2008).

Chapter 5 Properties of TlZnSnO film fabricated via sputtering of TlZnSnO target

5.1 Introduction

In this chapter, the fabrication of a TlZnSnO film is described, which is achieved via sputtering of a TlZnSnO target composed of TlZnSnO powder that is prepared using the two-step calcination process introduced in Chapter 4. As this is the first trial of TlZnSnO film preparation, not only the electrical properties, optical properties, and atomic concentration of the resultant film are reported, but also the band structure. In Chapter 3, the optical and electrical properties of the TlZnSnO film were predicted based on first-principles simulations. Therefore, the measured results of the optical property analyses are compared with the simulated results for TlZnSnO films with the same Tl content. Then, the author discusses the potential of TlZnSnO film for high mobility, the current problems, and the appropriate methods that should be applied in order to confirm various film properties. Finally, suggestions of refinements to the TlZnSnO fabrication process are made, with a view to improving the film properties.

5.2 Experimental

5.2-1 TlZnSnO target fabrication

The raw materials, i.e., ZnO (99.99%), SnO_2 (99.99%), and Tl_2O_3 (99.9%) powders were provided by Kojundo Chemical Laboratory Co., Ltd. The particle size was approximately 1 μm. To fabricate the TlZnSnO tablets, the author employed the two-step route shown in Fig. 4-1 (b). Tl_2O_3 and pre-prepared ZnSnO powders were used, where the ZnSnO powders were obtained through calcination of ZnO and SnO_2 at 1000 ºC for 24 h under atmosphere. The cation composition was controlled to 10.7 at.% Tl, 35.7 at.% Zn, and 53.6 at.% Sn. Binary powders with a total weight of 2 g were mixed using an agate mortar and pestle, and then pressed into pellets with 10-mm diameter and 1–2-mm thickness at 20 MPa. The pellets were sealed in a quartz ampoule under an air atmosphere of 0.03 MPa. The ampoule was then heated to 600 ºC, and this temperature was maintained for 18 h. The author wore a fine filtering mask during the process, from the TlZnSnO powder stage to the TlZnSnO target formation. The TlZnSnO sputtering target was fabricated by pressing TlZnSnO powder onto a stainless steel dish with a diameter of 2”. The initial pressure was set to 19.8 MPa/cm^2, and pressure was applied until the pressure gauge indicated saturation.

5.2-2 Sputtering conditions

The author employed three-target co-sputtering equipment produced by Kenix Co., which is shown in Fig. 5-2. The chamber walls and all parts of the chamber were covered with Al foil, which was selected based on the fact that Ar/O_2 plasma was used in the sputtering process. This prevented contamination of the Tl during sputtering. A previously prepared TlZnSnO ceramic target with 2”-diameter on a stainless steel dish was sputtered using radio-frequency (RF) plasma at room temperature for 1 h. Hence, several TlZnSnO films were fabricated on p-type crystal Si wafer (C-Si), SiO_2 film (100 nm) on C-Si, or alkali-free glass substrate. The p-type crystal Si wafer resistance was 0.5 Ω/□. The sputtering gas was a mixture of Ar and O_2, the total pressure of which was controlled at 10 or 1 Pa. These depositions were conducted under various O_2 partial pressure ratios of 5–50 %. The sputtering conditions were labeled A–D, corresponding to sputtering gas pressure and O_2 partial pressure ratios of 10 Pa:5 %; 10 Pa:25 %; 10 Pa:50 %; and 1 Pa:5 %, respectively. The distance between the target and the substrate was 50 mm, and the sputtering power was set to 10 W.

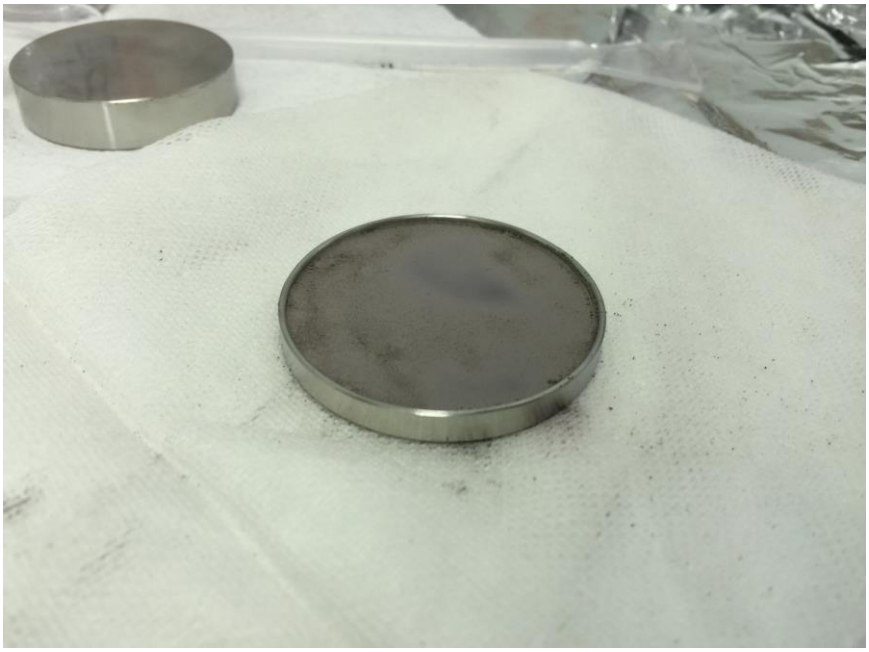

Fig. 5-1. TlZnSnO target.

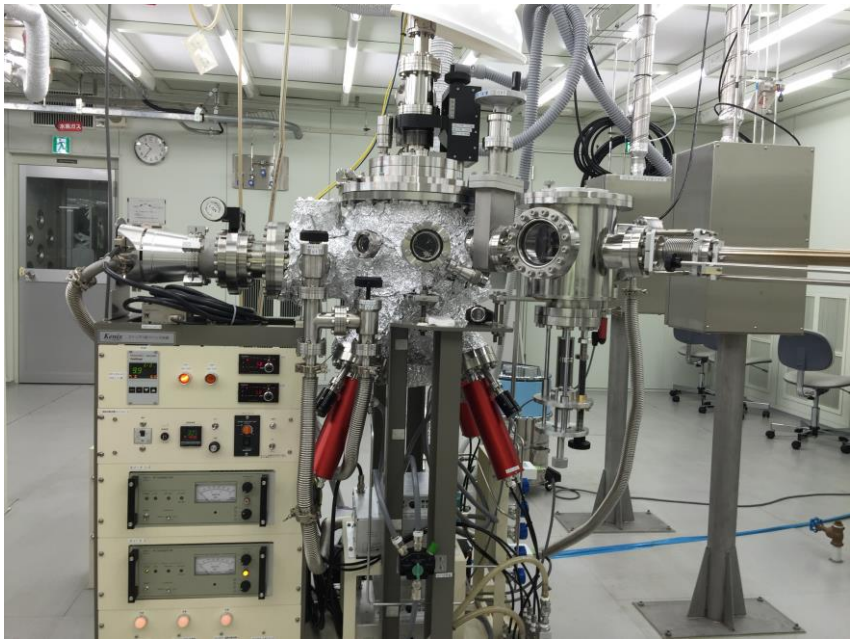

Fig. 5-2. Co-sputtering equipment with three targets.

5.3 Results and discussion

5.3-1. XRD profiles of TlZnSnO targets

The XRD profiles of the as-mixed ZnSnO +Tl_2O_3 (hereafter, TZTO-02) samples and those after 600 °C annealing for 18 h are shown in Fig. 5-3; these profiles confirm the previously obtained results. The XRD patterns for ZnO (card number: 00-036-1451), SnO_2 (card number: 00-041-1445), and Tl_2O_3 (card number: 00-033-1404) are also shown for reference. The results for the as-mixed and annealed samples were compared in order to confirm the volume change of the ZnO, SnO_2, and Tl_2O_3 crystals after annealing. This data could be obtained by comparing the Tl (222) peak with the Zn (101) or Sn (110) peaks. The Tl_2O_3-related peaks disappeared almost completely and the SnO_2 peaks were only slightly visible after the annealing; however, the Zn_2SnO_4 crystal peak was clearly apparent in the as-mixed sample and remained after the annealing with Tl_2O_3.

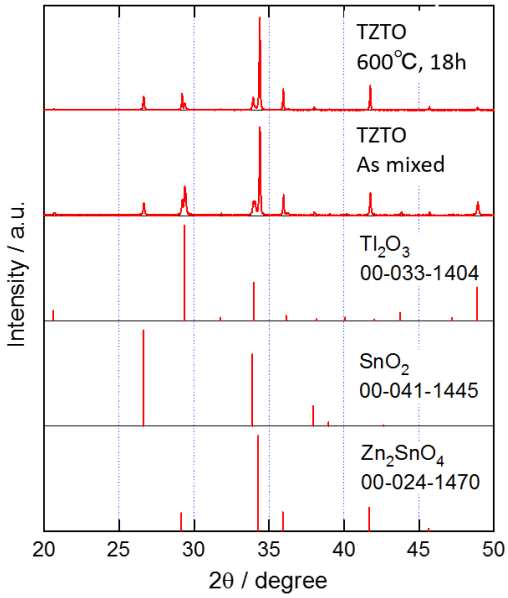

Fig. 5-3. XRD profiles of TZTO targets before and after calcination, with Tl_2O_3, SnO_2, and Zn_2SnO_4 profiles for reference.

5.3-2 Film thickness, density, and surface roughness of TlZnSnO films

The film thickness, surface roughness, and film density of each TlZnSnO film were measured and simulated through modeling of InZnSnO (IZTO)/SnO_2 (100 nm)/p+ Si via X-ray reflectometry measurement (XRR). Fundamentally, it is difficult to measure the thickness of a thin AOS, because of the lack of a sharp edge and the high transmittance. XRR measurement can be used to simulate the film density and surface roughness together. Therefore, XRR measurement was employed in order to obtain the film thickness. However, as the typical film properties of TlZnSnO are unknown, it was inevitable that the result for the TlZnSnO film thickness would involve some kind of scattering factor. Therefore, the author employed the typical film properties of IZTO in place of those of TlZnSnO. Table 5-1 shows the film thickness, the film density, and the surface roughness results for each film. As a

consistent total sputtering time of 1 h was employed in all cases, the film thickness and surface roughness values were decreased by increasing the O_2 partial pressure. The surface roughness values were approximately 0.5–1.4 nm; thus, the TlZnSnO films had larger surface roughness than InGaZnO (IGZO; approximately 0.3 nm). [1] In particular, those fabricated under conditions A and D (defined in subsection 5.2-2) had large surface roughness values of approximately 1.4 nm. These tendencies seem to depend upon a high plasma potential and a long mean free path for the sputtered particles. The film density was also reduced when the O_2 partial pressure was increased from 6.95 to 6.6 cm^{-3}, which is the same trend as for IGZO. [2] As the IGZO film density affects the film quality and, ultimately, the thin-film-transistor (TFT) stability [2], it is expected that a high-quality TlZnSnO film can be obtained at low O_2 partial pressure and low total pressure.

Table 5-1. XRR measurement results.

	A	B	C	D
Sample	10Pa 5%	10Pa 25%	10Pa 50%	1Pa 5%
Thickness(nm)	27.3	26.5	18.5	100
Density(g/cm3)	6.95	6.61	6.65	6.95
Roughness(nm)	1.4	0.5	0.6	2

5.3-3 Atomic concentrations of TlZnSnO films

The Tl concentration of each film was calculated from the XPS peak signal intensities for Tl, Sn, and Zn. The calculated values of the Zn, Sn, and Tl concentrations in each film are

shown in Fig. 5-4. All values are average results based on five measurements. The Zn/Sn ratio was slightly increased, from Zn/Sn = 3/2 in the target to Zn/Sn = 2/1 in the film. On the other hand, the Tl concentration was significantly reduced from ~10 to ~1 atom. %, indicating that the Tl concentration is more difficult to maintain than that of Zn or Sn during 600 °C calcination. As regards the Sn concentration, the unreacted and remnant SnO_2 (following the initial 1000 °C, 24-h calcination) was vaporized, and the Zn/Sn ratio became closer to that of the Zn_2SnO_4 compound. As regards the Tl concentration, this indicates that the Tl_2O_3 vaporization pressure was significantly larger than those of ZnSnO and SnO_2 during the 600 °C calcination. The Tl yield of the TlZnSnO fabricated from mixed powder comprised of Tl_2O_3 and ZnSnO was approximately 10 %, and it is thought that the remainder of the Tl atoms were vaporized and became attached to the quartz tube during the 600 °C calcination. However, it was also confirmed that the TlZnSnO films were sufficiently oxidized, based on the O concentrations in each film. Therefore, it was confirmed that the Tl reaction vapor was safely reduced in the air during calcination. Thus, there are no problems with regard to TlZnSnO target fabrication via 600 °C calcination in an air atmosphere.

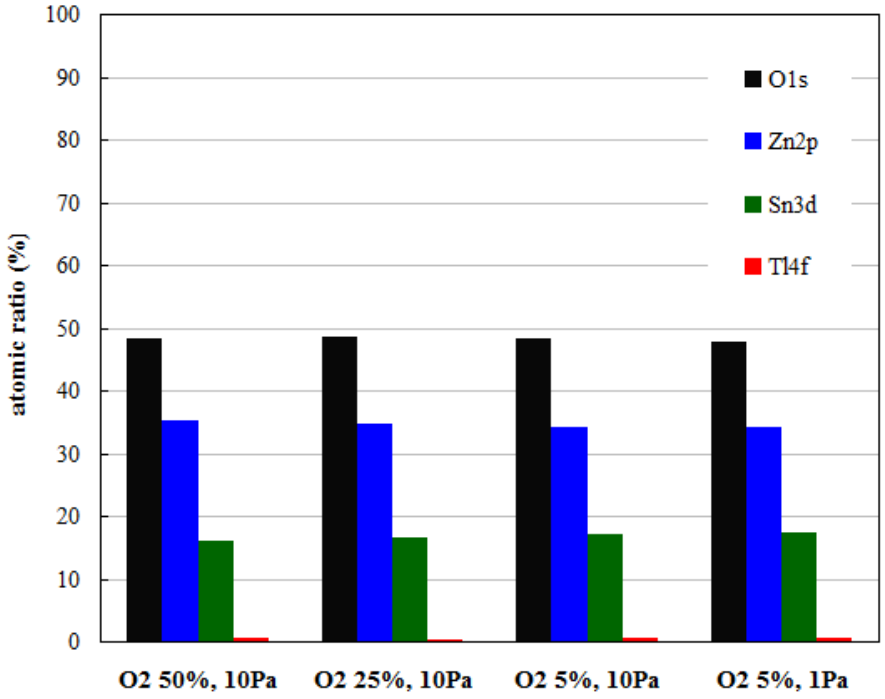

Fig. 5-4. Atomic concentrations of TlZnSnO films measured via XPS.

5.3-4 Optical characteristics of TlZnSnO

It was previously reported that IGZO film properties suitable for TFT applications were obtained under pressures of less than 1 Pa during sputtering. [3] For IGZO films obtained via direct current (DC) sputtering, an O_2 partial pressure of less than 10% was selected, as this value yields suitable film properties. [4] The author then attempted to estimate the pressure and O_2-partial-pressure dependence of TlZnSnO film properties during sputtering.

Optical bandgaps of 2.95 and 2.85 eV were obtained for the D and A conditions, respectively, as calculated from the Tauc plot. There is no significant difference between these results, which coincide with the energy bandgaps simulated via the first-principles method for Tl content of approximately 1%.

The O_2 partial pressure dependences of the optical bandgaps for conditions A–D are shown in Fig. 5-5. These bandgaps were calculated from the Tauc plots obtained via ellipsometry measurements, which indicate the quantity of light energy (hv) on the abscissa and the quantity of direct allowed transitions on the ordinate $(\alpha hv)^{1/2}$, where α is the absorption coefficient of the sputtered film. Under a total pressure of 10 Pa, the bandgap increased from 2.84 to 2.98 eV, when the O_2 partial pressure in the Ar/O_2 gas flow was increased from 5 to 50 %.

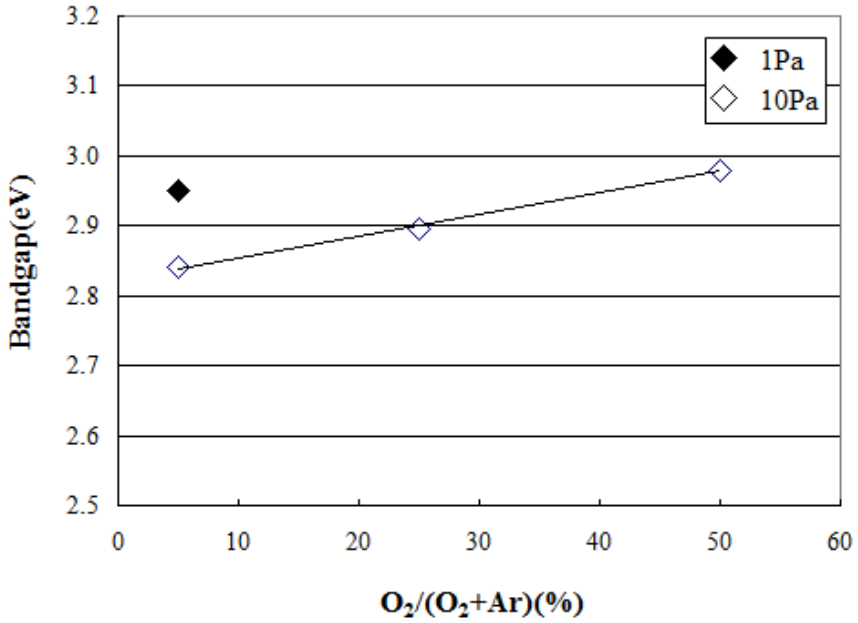

Fig. 5-5 O_2 partial pressure dependence of optical bandgap for 1 (blue diamonds) and 10 (solid diamond) Pa sputtering pressure.

The measured and simulated optical bandgaps are plotted in Fig. 5-6. The linear fit indicating the approximately linear relationship between the Tl concentration and energy bandgap in TlZnSnO obtained from the simulation was drawn according to

$y = 0.0305x + 2.86$ (eV), (5.1)

where y and x correspond to the energy bandgap and Tl concentration, respectively.

The measured bandgap results for the TlZnSnO films with Tl atom concentration values of 0.9–1.2 atom. % were distributed between 2.84 and 2.98 eV. The ZnSnO bandgap is 3.3 eV [5] and our simulation data indicate a similar value, based on the *y*-axis intersection (0 % Tl concentration) in Fig.3-3 (a). Further, the measurement results are closely distributed. As the simulation results were obtained for a film with no additional oxide deficiencies (Vo), it is thought that there were few Vo in the fabricated films, and that all the Zn, Sn, Tl, and O atoms in the TlZnSnO were sufficiently bonded for all films. In addition, all films were sufficiently oxidized, because they exhibited larger optical bandgaps compared with the results obtained from linear fitting of the simulated data.

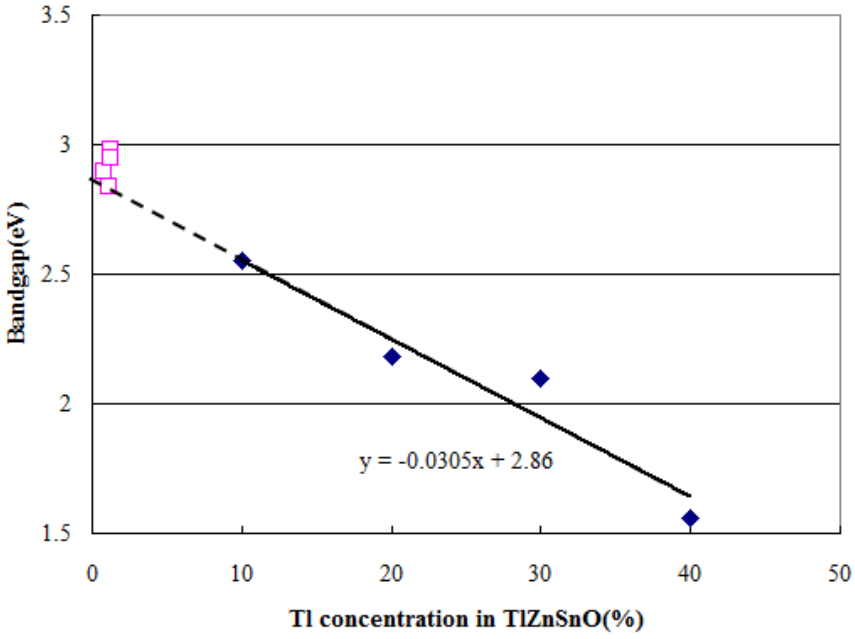

Fig. 5-6. Dependence of energy bandgap on Tl content of TlZnSnO according to simulation (blue diamonds) and measurement (magenta squares).

5.3-5 O and Tl bond stability in TlZnSnO film

XPS data were analyzed in order to compare the O and Tl bonds of the as-mixed samples with those of the annealed samples in the target. Hence, it was found that the Zn and Sn can contribute to improved Tl and O bonding stability, as indicated in Chapter 4. The same analysis was performed for each sample, and the XPS profiles of the Tl and O bonds in the TlZnSnO film are shown in Fig. 5-7. As in Chapter 4, the stabilities of the O and Tl bonds in the TlZnSnO film were estimated based on the XPS spectra of the O 1s and Tl 4f peaks. Two peaks can be observed for Tl 4f in Fig. 5-7 (a), indicating spin-orbit splitting to $4f_{7/2}$ and $4f_{5/2}$. The binding energies for $4f_{7/2}$ and $4f_{5/2}$ in Tl_2O_3 are approximately 117 and 122 eV, respectively [6], while the observed binding energies in the TlZnSnO film were 116.5 and 121 eV, respectively. The discrepancies are thought to be due to the presence of Tl_2O_3. In Fig. 5-7 (b), the TlZnSnO film O 1s profile appears to consist of three peaks, which have central positions of 528.5, 530, and 532 eV. Consequently, the peak resolution was conducted using Gaussian functions and the area intensity of each resolved spectrum was compared with the sputtering conditions, in order to evaluate the reactivity. The area intensity was also analyzed for the Tl $4f_{7/2}$ peak.

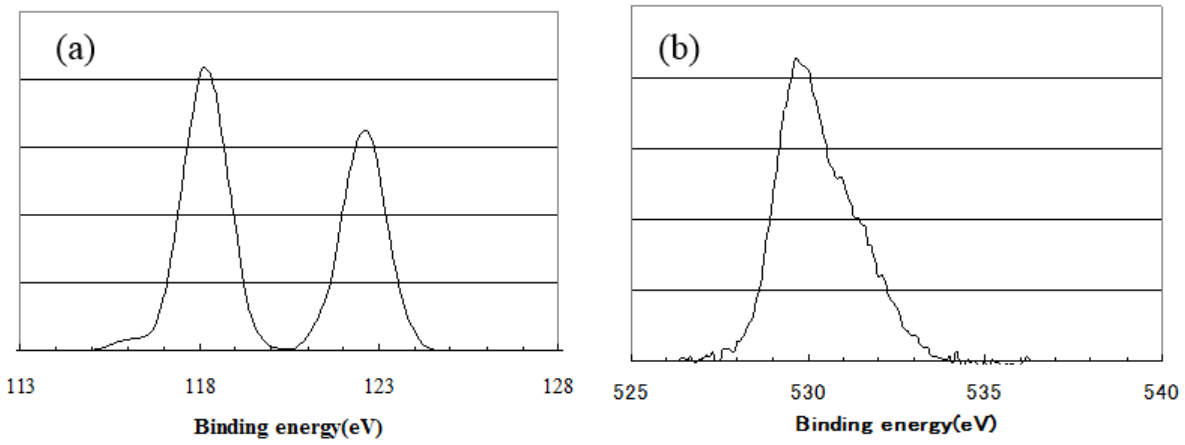

Fig. 5-7 XPS profiles of (a) Tl 4f and (b) O 1s in TlZnSnO film.

Figure 5-8 shows the O_2 partial pressure dependence of the (a) Tl and (b) O bonding ratios in TlZnSnO. For all preparation conditions, the main peaks of the profiles correspond to the $4f_{5/2}$ spin-orbit peak, the peak intensity of 118 eV (I_{118}) volume fraction of which is more than 90 %. On the other hand, small peaks corresponding to the $4f_{7/2}$ spin-orbit peak remain, the the peak intensity of 116.5 eV (I_{116}) volume fractions of which are less than 10 %. For the A–C preparation conditions, the I_{116} / (I_{116} + I_{118}) bonding ratio reduced from 4.6 to 2.5 % when the O_2 partial pressure was increased from 5 to 50 %. In contrast, for D, no peak corresponding to $4f_{7/2}$ was found, even under 5 % O_2 partial pressure. Thus, the Tl bond was stabilized under increased O_2 partial pressure and low-pressure sputtering. In particular, low-pressure sputtering yields a higher-stability Tl bond, as confirmed by the reduction in the I_{116} / (I_{116} + I_{118}) bonding ratio.

As regards the O 1s profiles, three peaks with volume fractions of I_{528}, I_{530}, and $I_{531.5}$ can

be identified in Fig. 5-7 (b). Under conditions A–C, the volume fractions at the lowest (I_{528}) and intermediate (I_{530}) energies decreased, while that at the highest energy ($I_{531.5}$) increased, as the O_2 partial pressure was increased from 5 to 50 %. In contrast, in the case of D, the spectral fraction at I_{528} is the lowest for the 10-Pa deposition, even under O_2 partial pressure of 5 %. Thus, similar to the Tl bond, the O bond was stabilized by increasing the O_2 partial pressure or by selecting low-pressure sputtering. Hence, low-pressure sputtering (~1 Pa) is more effective for decreasing weak Tl and O bonds than increasing the O_2 partial pressure.

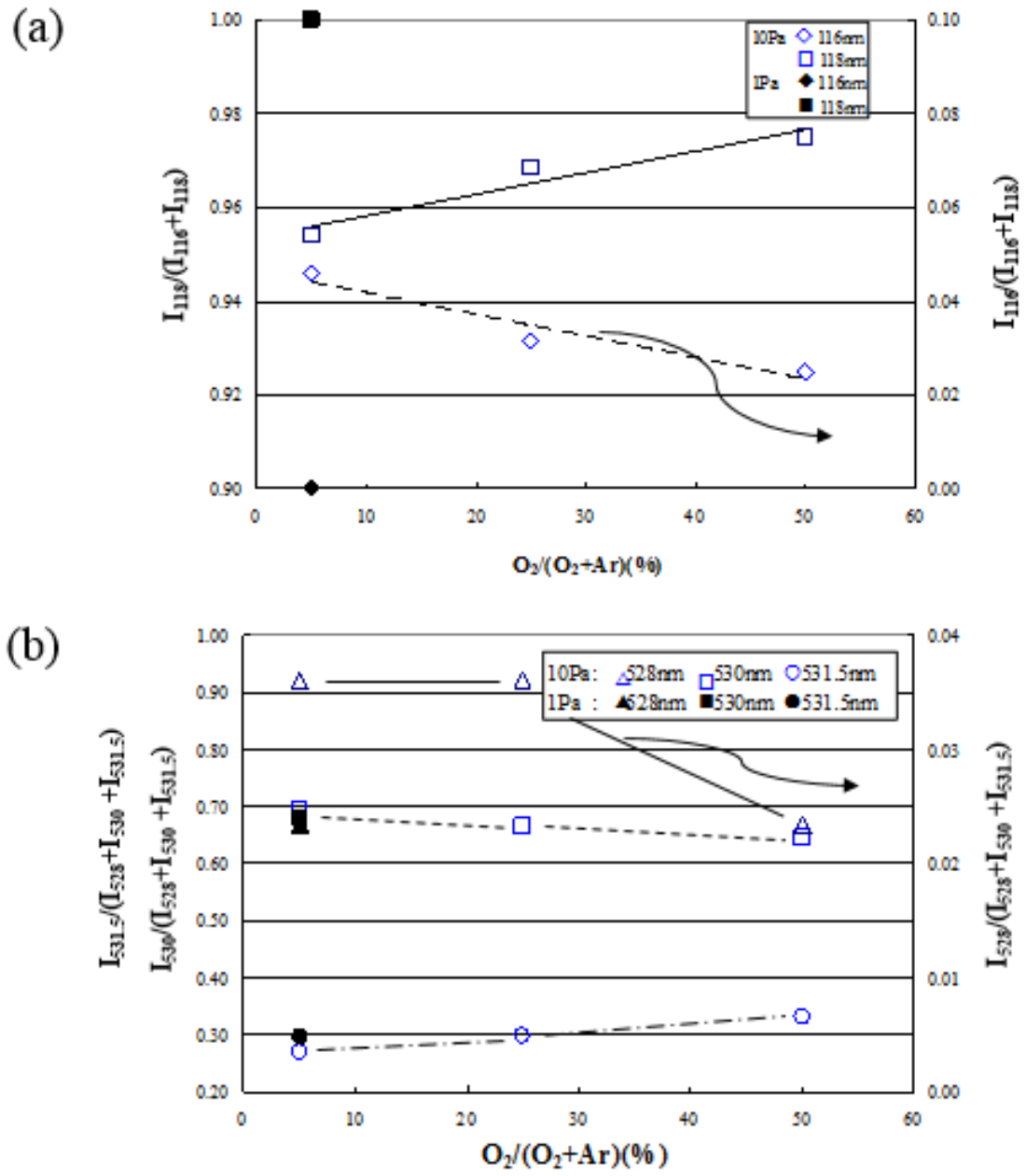

Fig. 5-8 O_2 partial pressure dependence of (a)Tl and (b) O bonding ratios in TlZnSnO.

5.3-6. Ionization potential measurement of TlZnSnO film

Photoelectron yield spectroscopy (PYS) using an ionized potential meter (AC-3, Riken Co.) was employed, in which the sample was irradiated by ultraviolet light, which excited the electrons via the photoelectric effect. The excited electron energies were recorded by a high-sensitivity ammeter. [7] In this technique, the current value indicated by the ammeter represents the work function and ionization potential of the examined semiconductor. Here, the measurements were conducted in an air atmosphere. The ionization potential of each film was measured using the PYS ionized potential meter, in order to determine the band structure thematic diagram of TlZnSnO. The relationships between the electron yield and photon energy for the films fabricated under conditions A–D are shown in Fig. 5-9, and each measured ionization potential is listed in Table 5-2. Three measurements were conducted for each sample and the average values were then obtained and compared. Linear regression was conducted, and the first slope of the regression line for the D case is lower than those for cases A–C. Second and subsequent measurements were conducted with the laser power being adjusted from 10 (black) to 20 μW (red), so as to obtain sufficient signal intensity. The signal dependence on the laser power was confirmed for powers between 10 and 20 μW for case D. There was no difference in the ionization potential for laser powers of 10–20 μW for cases A–C in Table 5-2.

These results clarify that the ionization potential depends on the O_2 pressure during

sputtering. Further, the ionization potential for case D is larger than those for A–C. The O_2 partial pressure dependences of both the optical bandgap and ionization energy are shown in Fig. 5-10. The unfilled squares (diamonds) show the optical bandgaps (ionization energies) for A–C. The filled square (diamond) shows the optical bandgap (ionization energy) for D. The ionization potential of IGZO has been reported as being more than 6 eV [8], while those of TlZnSnO are slightly smaller according to this measurement, at 5.57–5.9 eV. It is thought that the conduction band edge is located approximately 3 eV or more beneath the vacuum level in each case, and the higher film density for D is caused by the difference in the ionization energy compared to those for A–C.

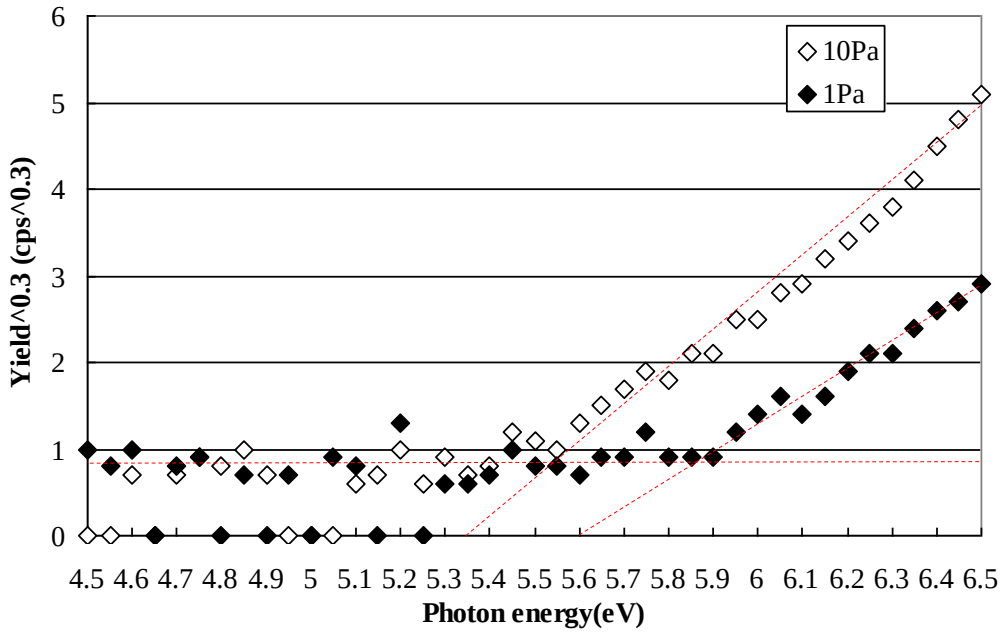

Fig. 5-9 Relationship between electron yield and photon energy for TlZnSnO films fabricated under 1 and 10 Pa.

Table 5-2. Ionization potentials of TlZnSnO films (black: 10 μW, red: 20 μW).

				(eV)
Sample	10Pa 5%	10Pa 25%	10Pa 50%	1Pa 5%
1st	5.56	5.65	5.66	5.93
2nd	5.57	5.68	5.67	5.87
3rd	5.59	5.69	5.67	5.89
Average	5.57	5.67	5.67	5.90

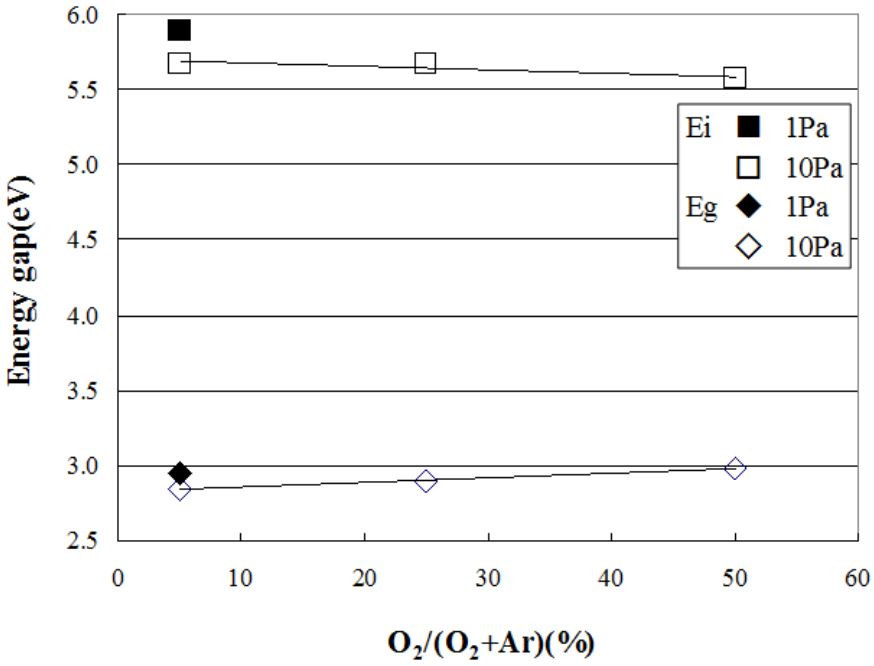

Fig. 5-10 O_2 partial pressure dependence of ionization energy and optical bandgap for 1- (unfilled) and 10-Pa (filled) sputtering pressure.

5.3-7. Temperature dependence of TlZnSnO film conductivity

The temperature dependences of the conductivities of TlZnSnO film specimens on Si/SiO_2 substrates with 100-nm thickness and 10×10 mm^2 surface area were measured by applying a voltage on an Mo coplanar electrode. The results for each film under the applied voltage (80–100 V) are shown in Fig. 5-11. The measurements were obtained at three different

positions on each sample and at 20-K intervals in the temperature range of 100–400 K. No significant discrepancies were obtained between the three values measured at each temperature. For A–C, the conductivities of all films increased continuously until a temperature of approximately 360 K was reached. Conventionally, the conductivity (σ) is expressed as

$$\sigma = \sigma_0 \exp(-Ea/k_B T), \quad (5.2)$$

and obtained via an Arrhenius plot, where σ_0 is a prefactor, Ea is the activation energy, k_B is the Boltzmann constant, and T is the temperature. The calculated results for each parameter of the Arrhenius plot, as obtained via a least-squares approximation, are shown in Table 5-3. The activation energies for A–C all exhibit the same value of 31 meV, displaying semiconductor characteristics with a 31-meV energy gap between the Fermi energy (E_F) and conduction band. The σ_0 for C was slightly higher than those for A and B. On the other hand, in the case of D, the conductivity was constant at approximately 1.5×10^{-2} ($\Omega^{-1}cm^{-1}$) up to 100 °C (380 K) and decreased continuously until 1×10^{-4} ($\Omega^{-1}cm^{-1}$) at 400 K. The electrical characteristics for the D case indicated resistance only, with no activation energy, and the carrier density rapidly decreased at temperatures higher than 380 K.

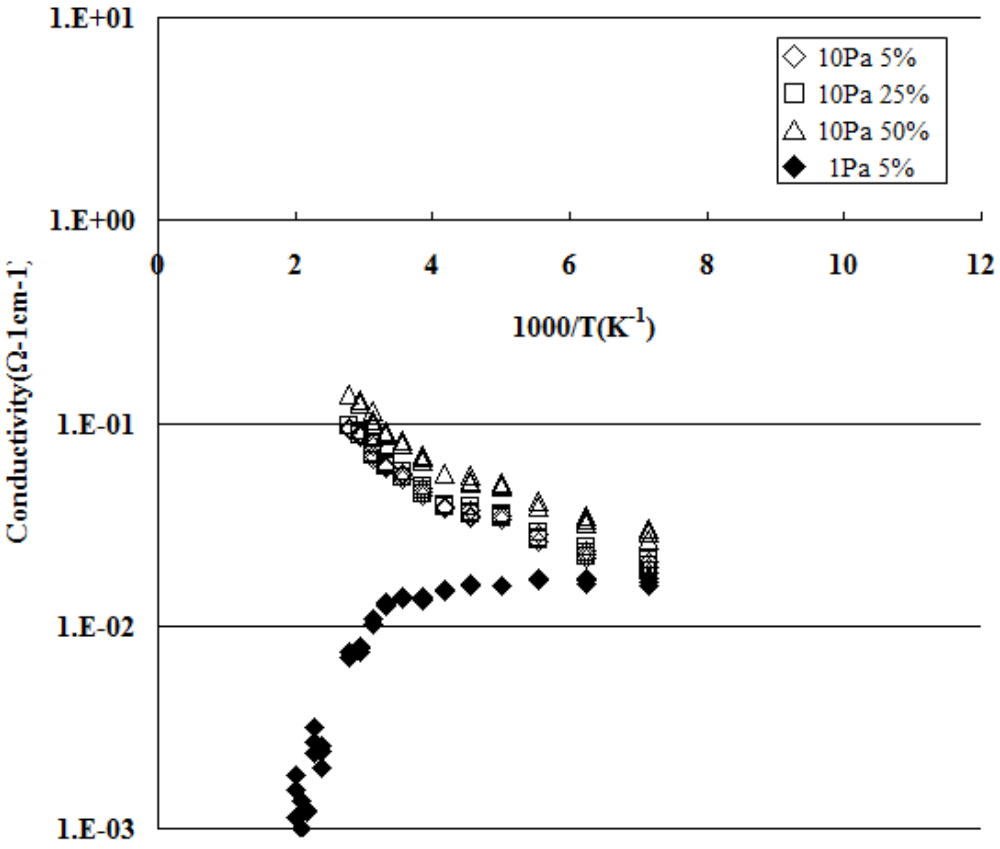

Fig. 5-11 Temperature dependence of TlZnSnO film conductivity.

Table 5-3. Arrhenius plot parameters for TlZnSnO films.

	ln(σ0)	Ea(meV)	σ0
10Pa 5%	-1.57	31	0.21
10Pa 25%	-1.54	31	0.21
10Pa 50%	-1.18	31	0.31

According to the results for IGZO shown in Fig. 5-12 [9] (from Kamiya et al.), the temperature dependence of the conductivity for the a2 and a3 samples with different deposition condition can be explained by the percolation conduction model. The author is of the view that a similar temperature dependence was exhibited by the TlZnSnO conductivity.

The results for the samples fabricated under the A–C conditions in this study are close to those for a2 in [9]. It has been reported that IGZO films with suitable semiconductor performance exhibit carrier densities of 10^{16}–10^{18} cm^{-3}. It is expected that a carrier density of approximately 10^{-17} cm^{-3} can be obtained for as-deposited TlZnSnO film, yielding a carrier mobility of more than 10 $cm^2V^{-1}s^{-1}$ in TFT applications.

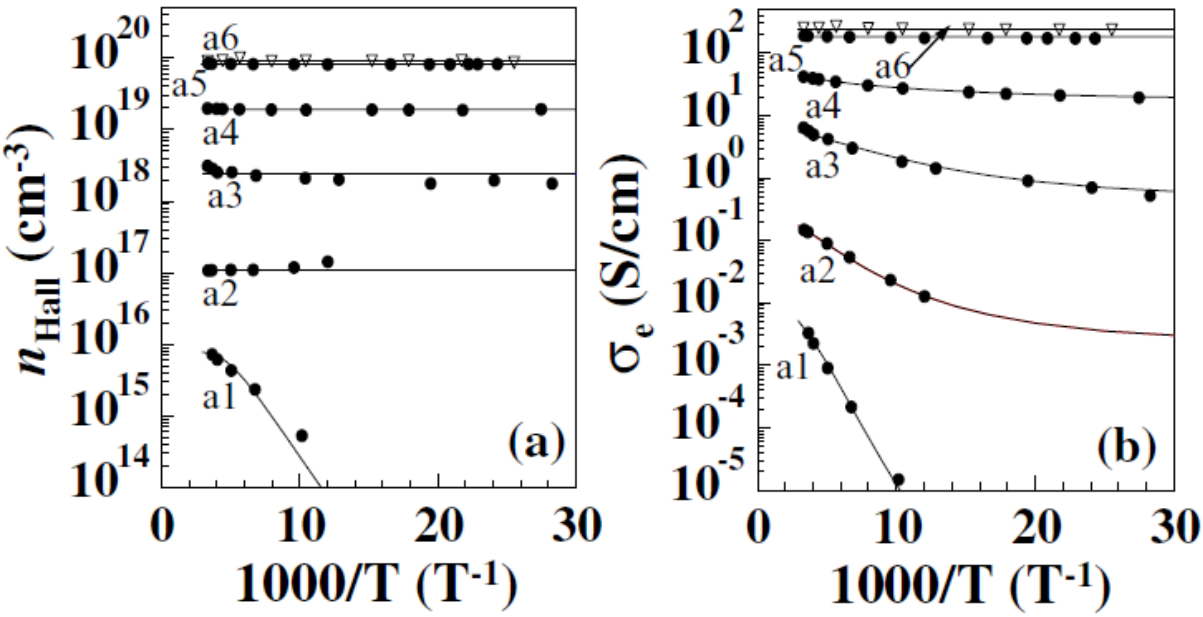

Fig. 5-12. Temperature dependences of (a) electron density and (b) conductivity for various amorphous IGZO films measured using the Hall effect. a1-a6 sample were fabricated under different deposition condition. The dots indicate experimental data and the solid lines were calculated using the percolation conduction model. [9]

5.3-8 TlZnSnO band diagram

The Hosono group has reported that the optical spectra of IGZO films provide information on the subgap density of states (DOS). [10] Fig. 5-12 shows the optical absorption spectra of various amorphous IGZO (a-IGZO) films. Here, HQ, LQ, as, and ann denote high-quality, low-quality, as-deposited, and annealed films, respectively. [11] The a-IGZO films have bandgaps of 3.0–3.2 eV; however, there is observable optical absorption in the photon energy range from 2.0 eV to the bandgap values. The widths of these subgap optical absorption features correspond well with the deep-subgap DOS above the valence band maximum (VBM) observed via hard X-ray photoemission spectroscopy (HX-PES) [12], and they are considered to have the same origin. In such a case, E_F is pinned in the subgap DOS and, thus, there should be no mobile holes in the valence band. According to a recent angle-resolved HX-PES (AR-HX-PES) study, the deep part of the DOS is primarily concentrated in the surface region [13]. It has also been reported that the deep-subgap DOS cannot be diminished via post annealing in a H_2O atmosphere.

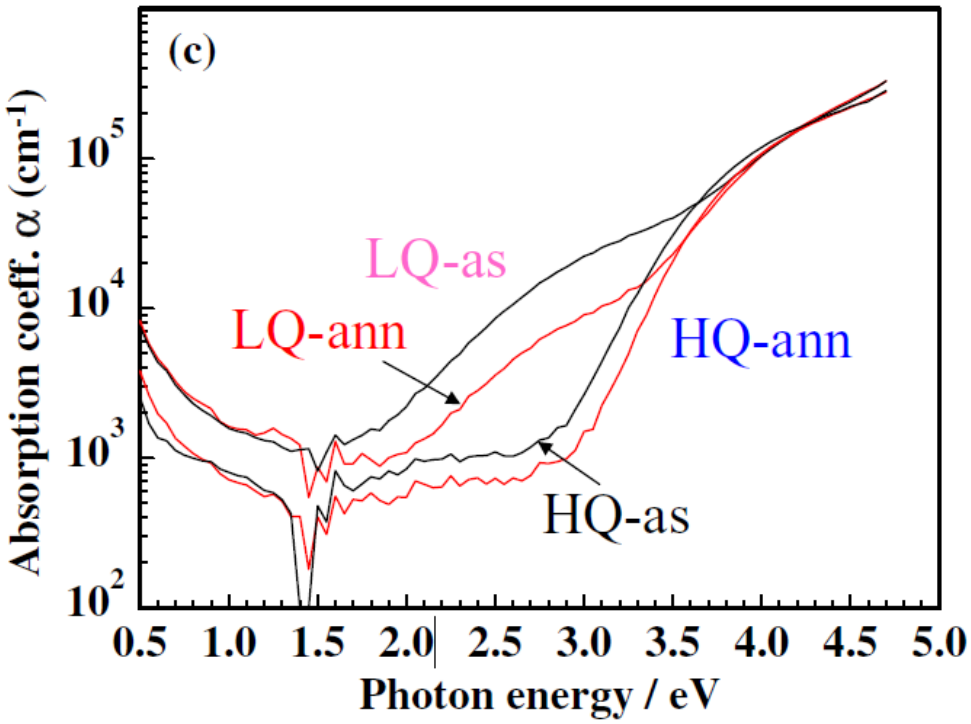

Fig. 5-13. Optical absorption spectra of various a-IGZO. HQ, LQ, as, and ann denote high-quality, low-quality, as-deposited, and annealed films, respectively. [12]

The author confirmed a similar trend for the film absorption coefficient, based on measurements conducted using an ellipsometer. A comparison between the Tauc plots of the optical spectra of the TlZnSnO films fabricated under conditions A and D is shown in Fig. 5-14. Considering the IGZO results, the absorption value of less than 3.7 eV for case D indicates a deep-subgap DOS above the VBM. This indicates poor film properties, as for IGZO. In contrast, no severe absorption under 3.7 eV is apparent for case A. Thus, superior film properties are expected for case A than for case D. However, as poor film properties appear for low-pressure conditions in common IGZO, this result indicates that TlZnSnO exhibits an opposing trend to IGZO. That is, TlZnSnO films fabricated via sputtering under

condition A exhibit less absorption near the VBM than those fabricated under condition D. For D, the additional absorption peak under 3.7 eV corresponds to 2.0-eV width. Thus, it is thought that a large DOS with a bandgap width of 2.0 eV exists for a LQ surface as shown in Fig. 5-14. It is speculated that both the roughness of the film surface and the Vo density are also significantly influenced by the deep-subgap DOS above the VBM. Thus, it is necessary to confirm the source of the TlZnSnO trend that is opposite to that for IGZO, along with the origin of this behavior, through HX-PES analysis.

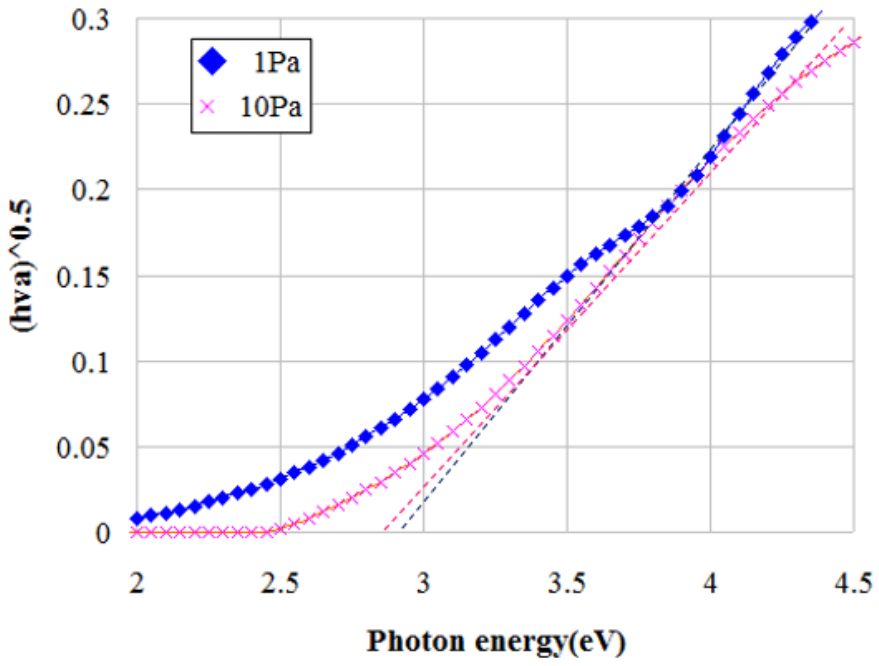

Fig. 5-14 Tauc plot of TlZnSnO optical data for
1- (blue diamonds) and 10-Pa (magenta crosses) sputtering pressure.

Finally, the band structure of TlZnSnO was determined, based on the results obtained above. Figure 5-15 is a schematic energy band diagram for the as-deposited TlZnSnO film. A

similar subgap DOS to that of a-IGZO is revealed for TlZnSnO; however, some differences exist. Specifically, the bandgap (2.84–2.95 eV) and donor level (31 meV) of TlZnSnO are smaller than those of a-IGZO, and a relatively wide deep level that is due to the surface DOS exists. It can be inferred that the deep-level DOS due to the surface properties has a significant influence on the semiconductor characteristics.

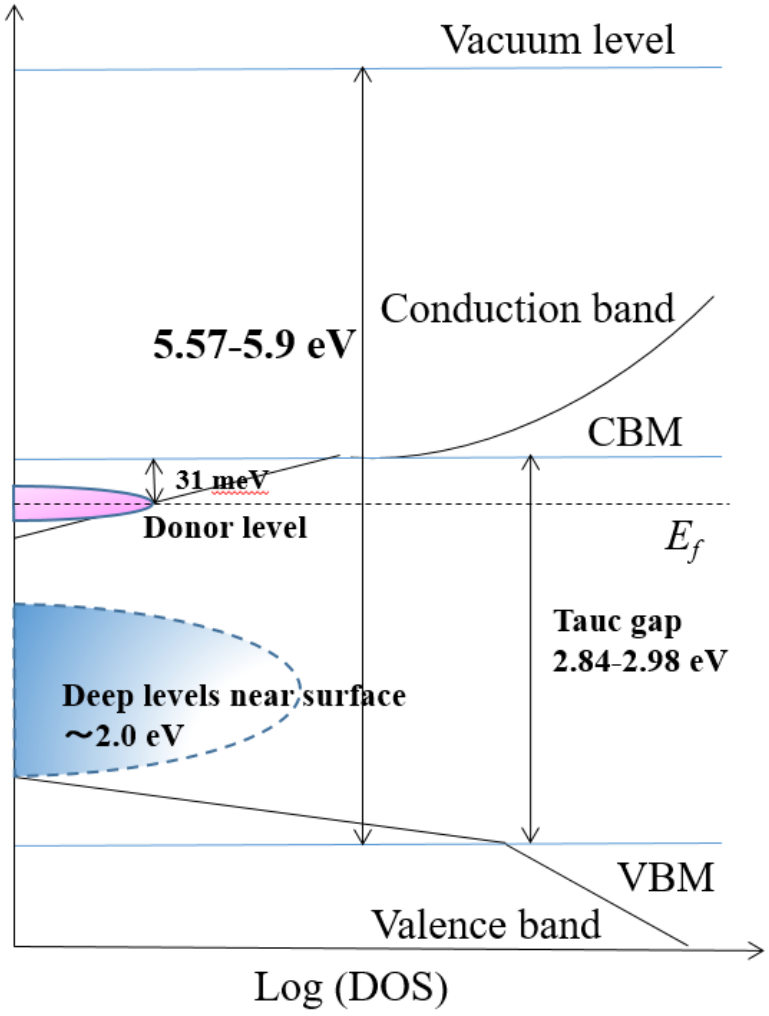

Fig. 5-15. Schematic model of subgap DOS in as-deposited TlZnSnO.

5.4 Future research

The optical and electrical properties and film structures of TlZnSnO films fabricated under several different sputtering conditions were discussed above. As this research into TlZnSnO film is still in the early stages, the film preparation technique is not sufficiently refined to allow estimation of the potential suitability of TlZnSnO for use in TFTs. In this section, some possible methods of confirming the feasibility of TlZnSnO films for such applications are suggested, and essential study and analysis prior to future TFT fabrication are discussed.

5.4-1 Determining suitable TlZnSnO atomic concentration for high-mobility TFTs

The author confirmed the Tl atom yield from Tl_2O_3 to TlZnSnO film for the original target fabrication using two-stage calcination. The Tl atomic content of the target was set to approximately 10 atom.% for comparison with $In_{0.4}$ZnSnO, because the m^* reduction achieved by adding Tl to ZnSnO was more than three times greater than that for added In, as shown in Chapter 3. However, the actual Tl concentrations in the films were only approximately 1%. Nevertheless, the film conductivities were relatively high, and are sufficient for the achievement of relatively high mobility and carrier density without a

post-annealing process. Therefore, in the future, it will be necessary to prepare TlZnSnO with more than 10 atom. % Tl content, because it is easy to compare the properties of this material with IZTO or IGZO semiconductor characteristics. From the simulation conducted in Chapter 3, a $Tl_{0.4}ZnSnO$ TFT is expected to achieve the highest TFT mobility of more than 50 $cm^2V^{-1}s^{-1}$, as the highest IZTO mobility was confirmed for the $In_{0.4}ZnSnO$ TFT.

5.4-2 Suitable TlZnSnO-film sputtering process for TFT fabrication

It was found that high total pressure and low O_2 partial pressure are required in order to prepare high-quality TlZnSnO. However, this trend is contrary to that for the common IGZO case. Thus, the author most confirm the optimal TlZnSnO process conditions in detail.

A smooth surface is an important parameter as regards TFT fabrication [10], and the surface roughness dependence on the various sputtering conditions must be confirmed. The measured surface roughness values of approximately 0.5–1.4 nm were larger than that of InGaZnO (~0.3 nm). [10] In particular, the surface roughness values were large (~1.4 nm) for low O_2 partial pressure, which was expected to yield superior film properties. As regards the surface roughness of AOS films, detrimental influences should be carefully monitored in order to ensure suitable properties for TFT fabrication. Thus, adjustments to the sputtering conditions that can yield improved smoothness must be considered. The film surface morphology should be analyzed via atomic force microscopy (AFM) measurement. This is

also an important technique as regards analysis of the surface roughness dependence on the Tl concentration.

5.4-3 Annealing effects on TlZnSnO film properties

Only a small number of the TlZnSnO film properties were examined as functions of the deposition conditions. The annealing process is key factor that determines the surface oxidation and bulk carrier density in AOS film. [13] Several types of annealing process that dramatically improve AOS film properties have been reported. [14] [15] Thermal post annealing yields a large load for mass production, but requires a long process time of approximately 1 h and a large oven with high electricity consumption. Therefore, not only thermal annealing, but also Ar plasma treatment should be examined. The latter may achieve the same effect [16], but with a significantly shorter process time of several dozen seconds and easy preparation using large-sized chemical vapor deposition (CVD) or etching equipment. In addition, multi-cathode/anode equipment such as that shown in Fig. 5-15 can be useful as regards improving the mass production. [17] [18] The illustrated chamber has several sets of cathodes (label 2) and anodes (4) with heaters (14), and can the production throughput can be increased significantly via parallel operation in the same chamber. In this figure, labels 12 and 7 indicate an RF generator and the feed-through, respectively, which can be discharged and can control the multi-plasma conditions simultaneously. The gas inlet tubes

(10) serve as gas supply sections and supply reactive material gas into the chamber. [17]

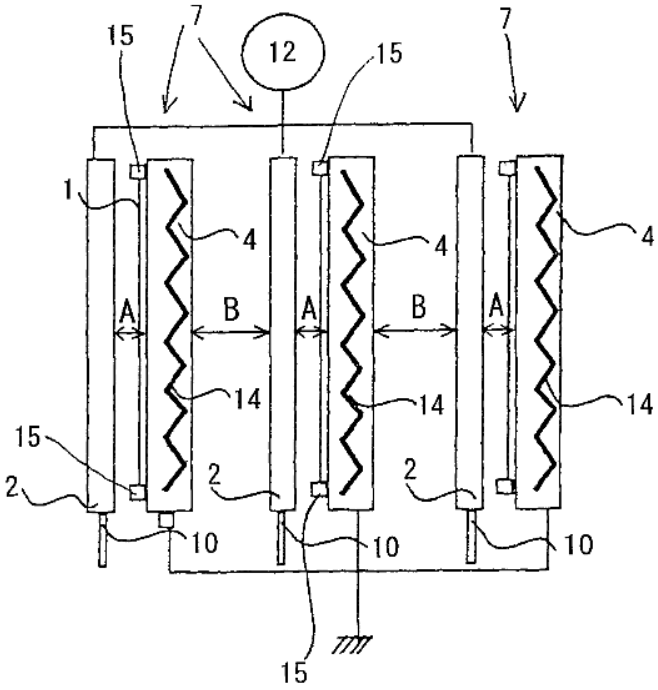

Fig. 5-15 Schematic longitudinal sectional view of plasma processing apparatus (with grounded anodes) . A is the electrode distance between anode and cathode. B is that of neighbor cathode-anode set. [18]

Annealing of the TlZnSnO films has not been attempted, but it is interesting to analyze the change in the electrical properties between the as-deposited and post-annealed TlZnSnO films. It is well-known that post annealing of AOS affects the surface oxidization to a depth of several dozen nanometers only. In the results of this study, one of the most interesting post-annealing effects is which the deep-subgap DOS above the VBM for film fabricated under condition D diminished or not by such as plasma treatment.

5.5 Conclusion

TlZnSnO films fabricated from sputtered TlZnSnO targets composed of TlZnSnO powder, which was prepared via two-stage calcination, were analyzed. As this study reports on the first trial of TlZnSnO film preparation, not only the electrical properties, optical properties, and atomic concentration were reported, but also the band structure. These characteristics were primarily compared with those of IGZO films.

The film properties and band structure of TlZnSnO were clarified based on the following results.

(1) The surface roughness values were approximately 0.5–1.4 nm, and were larger than that of IGZO, which is approximately 0.3 nm. In particular, the TlZnSnO films fabricated under low O_2 partial pressure had large surface roughness (~1.4 nm). The film density was also reduced in response to increased O_2 partial pressure, from 6.95 to 6.6 cm^{-3}, which is the same trend as for IGZO.

(2) The Tl concentration of each film was measured based on the XPS peak signal intensities of Tl, Sn, and Zn. The Zn/Sn ratio was increased slightly, from Zn/Sn = 3/2 to Zn/Sn = 2/1. On the other hand, the Tl concentration was reduced significantly from approximately 10 atom. % in powder form to approximately 1 atom. % in film form, when the TlZnSnO films were fabricated from TZO+Tl_2O_3 powders.

(3) The measurement results for the TlZnSnO film bandgaps for Tl atom concentrations of 0.9–1.2 atom. % were distributed between 2.84 and 2.98 eV. Our simulation data also indicate a similar bandgap, and the measurement results are closely distributed.

(4) As well as the Tl bond, the O bond was stabilized by increasing the O_2 partial pressure or by selecting low-pressure sputtering. Therefore, low-pressure sputtering at approximately 1 Pa is a more effective means of decreasing weak Tl and O bonds than increasing the O_2 partial pressure.

(5) The TlZnSnO ionization potential of 5.57–5.9 eV is slightly smaller than that of IGZO. As regards the band structure, the conduction band is located approximately 3 eV or lower beneath the vacuum level for each examined film, and a deep DOS state exists near the valence band.

(6) A similar subgap DOS to that of a-IGZO has been revealed for TlZnSnO. However, the bandgap (2.84–2.95 eV) and donor level (31 meV) of TlZnSnO are smaller than those of a-IGZO. A relatively wide deep level exists, which is due to the surface properties. It can be inferred that this surface-induced deep level influences the semiconductor characteristics. IGZO films with suitable semiconductor performance for use in TFT have been reported as exhibiting carrier densities of 10^{16}–10^{18} cm^{-3} [9], and it is expected that a carrier density of 10^{-17} cm^{-3} can be obtained for as-deposited TlZnSnO film, yielding more than 10 $cm^2V^{-1}s^{-1}$ carrier mobility in TFT applications.

References:

[1] Chapter 2-3 Structure of a-IGZO, H Hosono, M Hirano, Transparent Oxides and Active Electric Materials and Their Applications, 106 (2006).

[2] Room-temperature fabrication of transparent flexible thin-film transistors using amorphous oxide semiconductors, K Nomura, H Ohta, A Takagi, T Kamiya, M Hirano, H Hosono, Nature 432, 488 (2004).

[3] Processing effects on the stability of amorphous indium gallium zinc oxide thin-film transistors, H Q Chiang, B R McFarlane, D Hong, R E Presley, J F Wager, Journal of Non-Crystalline Solids, Volume 354, Issues 19–25, 2826 (2008).

[4] Application of DC magnetron sputtering to deposition of InGaZnO films for thin film transistor devices, O-K Moon, S Lee, D-H Kim, D-H Lee, C-O Jeong, J-W Park, Japanese Journal of Applied Physics 48, 031301 (2009)

[5] Origin of the improved mobility and photo-bias stability in a double-channel metal oxide transistor, H Y Jung, Y Kang, A Y Hwang, C K Lee, S Han, D-H Kim, J-U Bae, W-S Shin, J K Jeong, Scientific Reports 4, 3765 (2014).

[6] G E Muienberg, Handbook of X-ray Photoelectron Spectroscopy, Perkin-Elmer Corporation, (1979).

[7] Study of electronic structure and film composition at the back channel surface of amorphous In-Ga-Zn-O thin films, A Hinoz, T Kishi, H Tao, S Morita, K Hayashi, T Kugimiya, ECS Journal of Solid State Science and Technology volume 2, issue 4, 156 (2013).

[8] Electronic structure of the amorphous oxide semiconductor a-InGaZnO4–x: Tauc–Lorentz optical model and origins of subgap states, T Kamiya, K Nomura, H Hosono, Physica Status Solidi, Volume 206, Issue 5, 860 (2009).

[9] Present status of amorphous In–Ga–Zn–O thin-film transistors, T Kamiya, K Nomura, H Hosono, Science and Technology of Advanced Materials 11, 044305 (2010).

[10] Amorphous oxide semiconductors for high-performance flexible thin-film transistors, K Nomura, A Takagi, T Kamiya, H Ohta, M Hirano, H Hosono, Japanese Journal of Applied Physics 45, 4303 (2006).

[11] Origins of high mobility and low operation voltage of amorphous oxide TFTs: Electronic structure, electron transport, defects and doping, T Kamiya, K Nomura, H Hosono, Journal of Display Technology, Volume 5, Issue 7, 273 (2009).

[12] Depth analysis of subgap electronic states in amorphous oxide semiconductor, a-In-Ga-Zn-O, studied by hard x-ray photoelectron spectroscopy, K Nomura, T Kamiya, E Ikenaga, H Yanagi, K Kobayashi, H Hosono, Journal of Applied Physics 109, 073726 (2011).

[13] Trap densities in amorphous- In Ga Zn O 4 thin-film transistors, M Kimura, T Nakanishi, K Nomura, T Kamiya, H Hosono, Applied Physics Letters 92, 133512 (2008).

[14] The effect of annealing on amorphous indium gallium zinc oxide thin film transistors, H-S Bae, J-H Kwon, S Chang, M-H Chung, T-Y Oh, J-H Park, S Y Lee, J J Pak, B-K Ju, Thin Solid Films, Volume 518, Issue 22, 6325 (2010).

[15] Effect of high-pressure oxygen annealing on negative bias illumination stress-induced instability of InGaZnO thin film transistors, K H Ji, J-I Kim, H Y Jung, S Y Park, R Choi, U K Kim, C S Hwang, D Lee, H Hwang, J K Jeong, Applied Physics Letters 98, 103509 (2011).

[16] Improvements in the device characteristics of amorphous indium gallium zinc oxide thin-film transistors by Ar plasma treatment, J-S Park, J K Jeong, Y-G Mo, H D Kim, S-I Kim, Applied Physics Letters 90, 262106 (2007).

[17] Plasma processing apparatus with an exhaust port above the substrate, K Kishimoto, Y Fukuoka, US8395250 B2.

[18] Plasma processing apparatus, K Kishimoto, Y Hukuoka, US 7927455 B2.

Summary and outlook

In this study, the author has considered an effective solution to the problem of low mobility and V_O instability in In-based oxide semiconductors, and introduced the possibility of a Tl-based oxide semiconductor that can be used as a channel material for high-mobility and high-stability TFTs. Particular focus was placed on TlZnSnO TFTs.

The author experimentally confirmed that the size of the s orbital of element X in XZnSnO (X = Al, Zn, and In) obtained using a co-sputtering system strongly affects the TFT mobility. Then, the potential characteristics of TlZnSnO materials were predicted by estimating the TFT mobility based on those of AlZnSnO, GaZnSnO, and IZTO.

In addition, the author studied the potential TlZnSnO TFT performance using a first-principles simulation, in which the electron effective masses of IZTO and TlZnSnO were estimated. These results suggest that $Tl_{0.4}ZnSnO$ may have a high mobility of approximately 50 cm^2V^{-1} s^{-1}, owing to the emergence of the Tl 6s orbital with equal amounts of Zn and Sn. This high mobility is thought to be related to the Tl-Tl bond that appears in the case of Tl > 30 and 40 %, and it is believed that the 6s orbital of the Tl atom influences the high electron mobility via percolation conduction.

The thermal reactions between Tl_2O_3 and ZnO, SnO_2, or In_2O_3 annealed at 600 °C for 18 h in an air atmosphere were investigated. Tl_2O_3 had the largest reactivity with ZnO, which

clearly indicates that Zn_2SnO_4 has the same or higher reactivity against Tl_2O_3 than SnO_2 and ZnO mixed particles, despite the higher stability dispersion of the Zn and Sn atoms. Higher-stability TlZnSnO can be fabricated from Zn_2SnO_4+Tl_2O_3 powder via suitable thermal processes.

Finally, not only the electrical properties, optical properties, and atomic concentrations, but also the band structure of the TlZnSnO films were reported, primarily based on comparison with IGZO films. The film properties and band structure of the as-deposited TlZnSnO were determined based on the following results.

(1) The surface roughness values of approximately 0.5–1.4 nm were larger than that of InGaZnO, which is approximately 0.3 nm. The film density was also reduced when the O_2 partial pressure was increased from 6.95 to 6.6 cm^{-3}, which conforms to the trend for IGZO.

(2) The Tl concentration of each film was measured based on the XPS peak signal intensities of Tl, Sn, and Zn. The Zn/Sn ratio was slightly increased from Zn/Sn = 3/2 to Zn/Sn = 2/1. On the other hand, the Tl concentration was reduced significantly from ~10 atom. % in powder form to ~1 atom. % in film form.

(3) The Tl and O bonds were stabilized by increasing the O_2 partial pressure or selecting low-pressure sputtering. Therefore, low-pressure sputtering of approximately 1 Pa is more effective for decreasing weak Tl and O bonds than increasing the O_2 partial pressure.

(4) A similar subgap DOS to that of a-IGZO was revealed for TlZnSnO. However, some

differences exist. That is, the TlZnSnO bandgap (2.84–2.95 eV) and donor level (31 meV) are smaller than those of a-IGZO, and a relatively wide deep level due to the surface exists. IGZO films with suitable semiconductor performance have been reported to exhibit carrier densities of 10^{16}–10^{18} cm^{-3}, and it is expected that as-deposited TlZnSnO film will exhibit ~10^{-17} cm^{-3} carrier density, with more than 10 $cm^2V^{-1}s^{-1}$ mobility in TFT applications.

Acknowledgements

My heartfelt appreciation goes to Prof. Yukihiro Uraoka, who offered continuous support and constant encouragement that helped me to continue my doctoral studies for two years, despite the fact that I was living and working abroad. I am also deeply indebted to Associate Prof. Yasuaki Ishikawa, who was very understanding and supportive, and to Assistant Prof. Mami N. Fujii, who provided technical help and encouragement. As regards the TlZnSnO powder preparation, I am deeply grateful to Associate Prof. Yoshitaro Nose at Kyoto University, who studied the characteristics of the Tl reaction intensively and then provided helpful comments and suggestions. I am also heavily indebted to Kojundo Chemical Laboratory Co., Ltd., that prepared all the Tl_2O_3, ZnO, SnO_2, and In_2O_3 specimens used in this study.

I would like to express my deepest gratitude to Mr. Sakae Tanaka, whose comments and inestimably valuable suggestions motivated me in my studies. I would also like to thank Dr. Toshihiro Kugimiya at Kobelco Co., Ltd., whose detailed comments were extremely helpful to me. I would also like to thank Dr. Hyang-Shik Kong at Samsung Display Corp., who supported the early stages of my study, while I was employed at Samsung Display in Korea. I would also like to thank Dr. Dong-Hee Lee, Dr. Iljoon Kang, and Dr. Chang-Oh Jeong, who provided technical help and encouragement during the preparation of the simulation paper

based on this research.

I would also like to express my sincerest gratitude to my family: my wife, Tomomi, my three daughters, Rin, Sae, and Yu, and my parents, for their moral support and warm encouragement over the past two years.